



## Design, modeling, and characterization of a pulsed cold spray system

Ted Gabor<sup>a</sup>, Yijie Wang<sup>a</sup>, Semih Akin<sup>b</sup>, Fengfeng Zhou<sup>a</sup>, Jun Chen<sup>a</sup>, Yongho Jeon<sup>c</sup>, Martin Byung-Guk Jun<sup>a,\*</sup>

<sup>a</sup> School of Mechanical Engineering, Purdue University, 585 Purdue Mall, West Lafayette 47907, IN, USA

<sup>b</sup> Department of Mechanical, Aerospace and Nuclear Engineering, Rensselaer Polytechnic Institute, Troy, NY 12180, USA

<sup>c</sup> Department of Mechanical Engineering, Ajou University, Republic of Korea

### ARTICLE INFO

**Keywords:**  
 Pulsed cold spray  
 Cold spray  
 Numerical modeling  
 Computational fluid dynamics (CFD)  
 Particle image velocimetry (PIV)  
 Polymer metallization

### ABSTRACT

Pulsed cold spray (PCS) is a type of cold spray metal coating technique that incorporates cyclical compressed gas pulses to control the gas-powder for improved surface deposition. In recent years, PCS has garnered great attention owing to its unique pulsed nature in the domains of dense coatings, metal matrix composite coatings, cellular metallic structures, etc. However, research on the PCS to uncover process-structure-property relationships of this emerging deposition technique is limited. To this end, this study thoroughly investigates PCS to gain a deeper understanding of this coating technique. First, a PCS system incorporating a converging-diverging (CD) nozzle is designed and prototyped. Next, two-phase flow (i.e., gas + powder) within the PCS is modeled using computational fluid dynamics (CFD). The modeling results are then experimentally validated using particle image velocimetry (PIV), followed by a case study on surface deposition. The results show that the optimal powder injection window occurs when the gas inlet pressure is at least 99 % of the set inlet pressure, achieving a steady-state gas flow for 100 ms. CFD modeling showed that Mach diamonds formed at the nozzle exit by 30 ms, though powder velocity does not reach steady-state until 50 ms. Numerical modeling captured the average particle with an error of  $\approx 8\%$  as compared to the PIV measurements. Furthermore, surface deposition experiments showed that the PCS can create dense coatings with remarkably less porosity (i.e., 1.73-fold) as compared to the traditional CS. Overall, this study unravels the intricacies of designing and modeling of a PCS system with a CD nozzle, complemented by surface deposition experiments.

### Nomenclature

Symbol	Description
$A_p$	Particle cross sectional area ( $m^2$ )
$a$	Experimental parameters for Drag Coefficient
$C_D$	Drag Coefficient
$C_p$	Specific heat of air (1006.43 J.(kgK) $^{-1}$ )
$d$	Particle diameter ( $\mu m$ )
$\bar{d}$	Average particle diameter ( $\mu m$ )
$d_{50}$	Median particle diameter ( $\mu m$ )
$F_i, \vec{F}$	Force (N)
$\vec{g}$	Acceleration of gravity ( $m.s^{-2}$ )
$k_T$	Thermal conductivity of air (0.0242 W.(mK) $^{-1}$ )
$L$	Length (m)
$m$	Mass of air (kg)
$m_p$	Particle mass (kg)
$\dot{m}_p$	Particle mass flow rate ( $kg.s^{-1}$ )

(continued on next column)

(continued)

Symbol	Description
$M_p$	Particle Mach number
$n$	Rosin-Rammler diameter distribution parameter
$P$	Pressure (MPa)
$R$	Ideal gas constant (8.314 J.K $^{-1}.mol^{-1}$ )
$Re$	Gas Reynold's number
$Re_p$	Particle Reynold's number
$S$	Separation distance of DDA
$t$	Time (s)
$T$	Temperature (K, °C)
$T_{outlet}$	Measured nozzle outlet temperature (°C)
$u, v, w$	Cartesian velocity components ( $m.s^{-1}$ )
$w$	Width (m)
$V$	Volume of gas ( $m^3$ ); voltage (V)
$\vec{v}$	Gas velocity vector ( $m.s^{-1}$ )
$\vec{v}_p$	Particle velocity vector ( $m.s^{-1}$ )

(continued on next page)

\* Corresponding author.

E-mail address: [mbgjun@purdue.edu](mailto:mbgjun@purdue.edu) (M.B.-G. Jun).

(continued)

Symbol	Description
Abbreviation	Description
$x, y, z$	Cartesian positional components (m)
$\mu$	Viscosity of air ( $1.789 \times 10^{-5}$ kg.(ms) $^{-1}$ )
$\rho$	Density of air (kg.m $^{-3}$ )
$\rho_p$	Particle material density (kg.m $^{-3}$ )
Al	Aluminum
C	Carbon
CAD	Computer Aided Design
CCD	Charge-Coupled Device
CD	Converging-Diverging
CFD	Computational Fluid Dynamics
CS	Cold Spray
Cu	Copper
LPCS	Low Pressure Cold Spray
Nd:YAG	neodymium-doped yttrium aluminum garnet
PCS	Pulsed Cold Spray
PGDS	Pulsed Gas Dynamic Spraying
PIV	Particle Image Velocimetry
RT	Room Temperature
SEM	Scanning Electron Microscopy
Si	Silicon
Sn	Tin
WC	Tungsten Carbide

## 1. Introduction

Cold Spray (CS) – a metal coating and additive manufacturing process – uses supersonic gases such as air, nitrogen, and helium to accelerate metallic powders to high velocity [1]. When the powders reach a process- and material-specific critical velocity [2], they are deposited onto a metallic, polymer, or ceramic substrate, where the powders bond to the surface via mechanical interlocking and localized particle-substrate heating due to deformation and friction [3]. As a manufacturing process, CS has been used for coating, part repair, and additive manufacturing [2]. Furthermore, the low-process temperature of CS is ideal for uses in the functional metallization of polymer and composite substrates [4–9], as well as for the deposition of materials sensitive to high-temperature and oxidation [2,10,11].

Traditional CS process is a continuous flow process, where powder is sprayed at a constant powder feed rate with a controlled gas inlet temperature (25–800 °C) and pressure (0.5–5 MPa) [12]. This method may be undesirable in cases where gas or powder supplies need to be preserved, or where powder deposition efficiency is reduced due to required use of low gas pressures and temperatures. In these cases, the implementation of control valves to the gas and/or powder feeds is beneficial. The Pulsed Gas Dynamic Spraying (PGDS) is a type of Pulsed Cold Spray (PCS) process that uses controlled gas pulses to accelerate powders to critical velocity using shock-wave compression, where both the gas pulses and powder feed are controlled through precisely timed valve actuators [13,14]. Initially proposed by Jodoin et al. [13] and commercially known as Shockwave Induced Spraying (*Centerline SST*) [15], this process uses shockwave gas compression along with heaters to increase powder temperature and velocity, consequently improving deposition process. As such, it is possible to achieve denser coatings using PGDS compared to the continuous traditional CS process [13,14,16,17]. Notably, these nozzles are much longer than their traditional CS counterparts – the PGDS nozzle is 700–2250 mm long [13,18] while divergent length of traditional CS nozzles are only 50–300 mm long [18]. Additionally, the PGDS design incorporates a long, straight nozzle tube of constant diameter to ensure the constant strength of the shock wave in the nozzle [13], whereas traditional CS nozzles use a converging-diverging nozzle type [1,14].

PCS has been used to manufacture coatings for a variety of applications. Yandouzi et al. initially used the PGDS process to deposit dense

Tungsten Carbide (WC)-based conventional and nanocrystalline cermet coatings onto Al plates [18], which managed to preserve the microstructure of the cermet powders [19]. Additional studies performed by Yandouzi et al. focused on understanding the effects of powder material type, finding that the optimal process parameters are dependent on the type of cermet powder used [19]. Furthermore, Yandouzi and Jodoin studied the effects of the PGDS process parameters, finding that increasing the gas pressure and temperature above critical values reduced the amount of coating defects and improved substrate/coating interface quality [20]. Meanwhile, reducing standoff distance and increasing initial powder feed temperature improved deposition efficiency and reduced coating porosity [20]. PGDS has been also employed in the manufacturing of composite coatings, from WC-composite coatings [19], to aerospace carbon/epoxy composites [21], to Al-based metal matrix composites [16], and to SiC particle reinforced Al–12Si alloy composite coatings [17]. More recently, Nikbakht and Jodoin used the PGDS process to manufacture thick Cu-hBN coatings, which was challenging to produce using standard CS [22]. Nikbakht et al. also used PGDS to manufacture cellular metallic structures that have a porosity >70 % [23], demonstrating that pulsed sprays can be used for both sparse and dense coatings depending on the required application.

Initial modeling of the PGDS process was performed by Jodoin et al. [13], where 1D flow modeling predictions matched within 10–15 % of 3D modeling results. These results showed that helium allowed higher gas velocities and temperatures in comparison to air/nitrogen, and that peak velocities for helium were predicted to be above 1700 m/s at temperatures above 600 °C using high inlet pressure and temperature. Nitrogen and air, on the other hand, could only go above 700 m/s at temperatures above 450 °C. Further analysis was performed by Karimi et al. [24,25] using computational fluid dynamics (CFD) modeling. From the gas flow study [24], it was found that the unsteady nature of the process allowed for the higher velocity gas flows at higher temperatures compared to the standard CS process, as high-velocity steady-state flows produced by CS results in a lower outlet temperature compared to the inlet temperature. The length of the nozzle was also significant, as increasing the nozzle length improves the chance for the powders to stay within the high-speed pulse region. Raising the nozzle pressure also allowed for the pulse to stay within the nozzle for longer without dissipating and correspondingly raised the gas temperature due to increased compression within this region. Adding the particle phase [25] allowed for the model to predict deposition efficiency trends found from experimental analysis of the PGDS process, but suggests there is room for improvement in the powder injection modeling process.

The extensive literature discussed above has significantly advanced our understanding of the PCS process and identified pathways to enhance the efficiency of this technique. Nevertheless, there are still crucial knowledge gaps that need to be addressed, including:

- 1) Development and analysis of a PCS nozzle that incorporates: (i) a CD nozzle form factor; (ii) a powder feeding mechanism that incorporates a siphonage effect similar to a low-pressure cold spray nozzle [26]
- 2) In-depth modeling of 3D transient powder flow within the PCS featuring a CD nozzle
- 3) Analyses of dense and sparse coatings made using the PCS
- 4) Coating performance comparison of the PCS against traditional CS for polymer metallization applications

To address these knowledge gaps and to ensure continued progress towards a comprehensive understanding of this emerging technique, a PCS system with a CD nozzle is designed and prototyped. Afterwards, the two-phase gas-powder flow within the PCS is modeled by via numerical modeling to analyze and understand the gas flow dynamics and powder dispersion. The numerical modeling (i.e., CFD model) is then experimentally validated with Particle Image Velocimetry (PIV). Finally, surface deposition experiments were conducted via the PCS

system and its deposition performance compared against a traditional CS system. This study contributes to the advancement of PCS processes across various application domains.

## 2. Materials and methods

### 2.1. Prototyping of a pulsed cold spray (PCS)

**Fig. 1a-c** shows the computer-aided design (CAD) modeling of the PCS and its representative image, respectively. The PCS mainly consists of three sections, namely (i) stagnation chamber; (ii) pressure gauge port; and (iii) converging-diverging (CD) nozzle. The CD nozzle is attached to a large stagnation chamber 171.5 mm long with a radius of 38 mm. The stagnation chamber also includes a sloped converging section to ensure a smooth transition from the chamber to the CD nozzle. A pressure gauge is attached to the stagnation chamber with a flange connecting the high-pressure-rated (200 PSI/13.8 bar maximum), 120 V solenoid valve (ASCO Redhat). The dimensions of the nozzle prototype are outlined in **Table 1**.

The working mechanism of the PCS is presented in **Fig. 1d**. A computer provides and sends the code to a controller (*Arduino Uno*), which actuates the high-pressure-rated solenoid valve through a high-voltage relay based on a provided signal input. The solenoid valve opens and lets in pressurized air into the PCS nozzle, where it pressurizes a gas expansion chamber and accelerates the gas to a supersonic velocity.

**Table 1**  
PCS nozzle dimensions.

Total length (mm)	357.54
CD nozzle length (mm)	131
Convergent length (mm)	11
Throat diameter (mm)	2.5
Divergent length (mm)	120
Expansion ratio	3.68
Exit area (mm <sup>2</sup> )	18.1
Powder inlet diameter (mm)	1.5
Throat to powder inlet distance (mm)	6

Current inlet pressures tested for the PCS system range from 7 to 12.4 bar. Due to the high speed of the gas inside the nozzle, the pressure drops below atmospheric level, creating a siphonage effect that draws in powder from the powder feeder attached to the powder inlet port. This ensures that powders are drawn into the nozzle's main gas flow to be accelerated through the rest of the nozzle's divergent section. In these cases, a vibratory-based powder feed system such as ones provided by Dymet in their low-pressure CS systems [26] were employed for initial deposition testing. The powder feed rate for the PCS system was determined to be 1.125–1.375 g/pulse. The solenoid valve is used to actuate the gas flow by a 5 V DC to 120 V relay, connected to an *Arduino Uno* which runs an actuation code. The code is triggered by a push button (i.e., signal input) connected to a pullup resistor circuit (see **Fig. 1d**). When

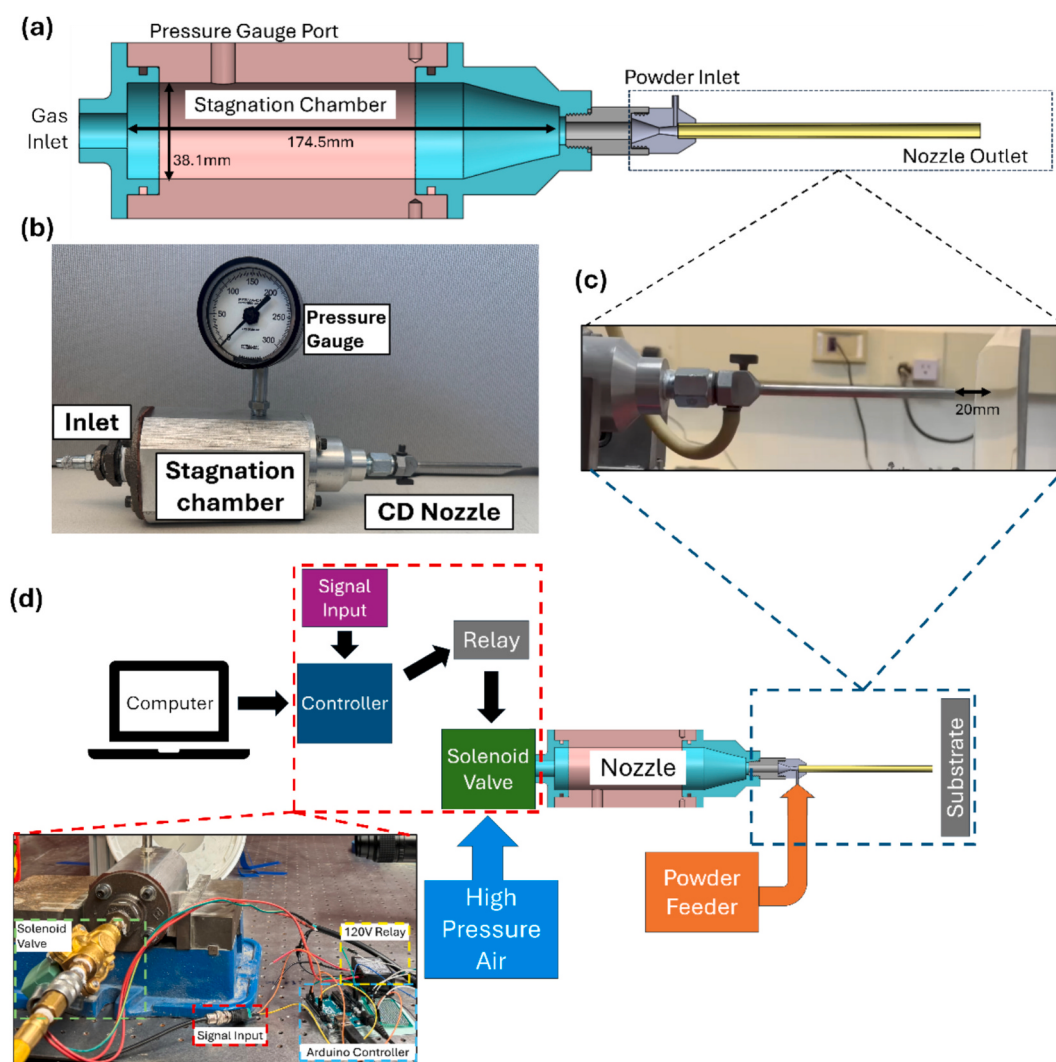


**Fig. 1.** PCS prototype overview, with (a) cross-sectional CAD model, (b) manufactured prototype, (c) CD nozzle closeup, and (d) PCS control and operational setup.

the button is pressed, or the controller receives a signal input from a timing device, the solenoid turns on and off in a specified 200 ms loop. Consequently, the powders are accelerated via the pulse spray created in a programmable manner.

## 2.2. Feedstock powders

The feedstock powder materials used for experimental analysis include both spherical Cu (*Chemical Store Inc.*) and quasi-spherical Sn powders (*Centerline SST*), whose morphologies are shown in Fig. 2. The sizes of each powder types in a range of 5–44  $\mu\text{m}$  [27], with a  $d_{50} = 36 \mu\text{m}$  for Cu and  $d_{50} = 17 \mu\text{m}$  for Sn powders, respectively. The Cu powder is used in both CFD modeling and validation experiments via PIV. Additional information regarding the Cu diameter distribution can be seen in Fig. S1 (supporting information). As for the surface deposition experiments, Sn powders were deposited on the AA6063-T5 aluminum alloy substrate (*The Hillman Group, Inc.*) with a thickness of 0.635 mm as well as the polyethylene terephthalate (PET) polymer target with a thickness of 0.25 mm. Compressed air was employed as the driving gas in both CFD simulations and experimental studies. All the materials are used as received without any further treatment.

## 2.3. Model overview

Given the time-dependent nature of the PCS system, a 3D RANS transient analysis of the gas-powder flow was implemented using ANSYS FLUENT 2022R2 using the Eulerian-Lagrangian scheme. The Eulerian gas phase was set to be an ideal gas air ( $PV = \frac{mRT}{M}$ ), where the molar mass of air is set to 28.966 g.mol $^{-1}$ , the specific heat ( $C_p$ ) of air was set to 1006.43 J.(kgK) $^{-1}$ , and the thermal conductivity  $k_T$  of air was set to 0.0242 W.(mK) $^{-1}$ . To properly model the gas flow phase, the continuity (Eq. (1)), Navier-Stokes (Eqs. (2)–(4)), and conservation of energy (Eq. (5)) equations were incorporated [28]:

$$\frac{\partial \rho}{\partial t} + \frac{\partial(\rho u)}{\partial x} + \frac{\partial(\rho v)}{\partial y} + \frac{\partial(\rho w)}{\partial z} = 0 \quad (1)$$

$$\rho F_x - \frac{\partial P}{\partial x} + \mu \left( \frac{\partial^2 u}{\partial x^2} + \frac{\partial^2 u}{\partial y^2} + \frac{\partial^2 u}{\partial z^2} \right) + \frac{1}{3} \mu \frac{\partial}{\partial x} \left( \frac{\partial u}{\partial x} + \frac{\partial v}{\partial y} + \frac{\partial w}{\partial z} \right) = \rho \frac{Du}{Dt} \quad (2)$$

$$\rho F_y - \frac{\partial P}{\partial y} + \mu \left( \frac{\partial^2 v}{\partial x^2} + \frac{\partial^2 v}{\partial y^2} + \frac{\partial^2 v}{\partial z^2} \right) + \frac{1}{3} \mu \frac{\partial}{\partial y} \left( \frac{\partial u}{\partial x} + \frac{\partial v}{\partial y} + \frac{\partial w}{\partial z} \right) = \rho \frac{Dv}{Dt} \quad (3)$$

$$\rho F_z - \frac{\partial P}{\partial z} + \mu \left( \frac{\partial^2 w}{\partial x^2} + \frac{\partial^2 w}{\partial y^2} + \frac{\partial^2 w}{\partial z^2} \right) + \frac{1}{3} \mu \frac{\partial}{\partial z} \left( \frac{\partial u}{\partial x} + \frac{\partial v}{\partial y} + \frac{\partial w}{\partial z} \right) = \rho \frac{Dw}{Dt} \quad (4)$$

$$\begin{aligned} \frac{\partial}{\partial t} (\rho C_p T) + \frac{\partial(\rho u C_p T)}{\partial x} + \frac{\partial(\rho v C_p T)}{\partial y} + \frac{\partial(\rho w C_p T)}{\partial z} = \\ \frac{\partial}{\partial x} \left( k_T \frac{\partial T}{\partial x} \right) + \frac{\partial}{\partial y} \left( k_T \frac{\partial T}{\partial y} \right) + \frac{\partial}{\partial z} \left( k_T \frac{\partial T}{\partial z} \right) \end{aligned} \quad (5)$$

where,  $u$ ,  $v$ , and  $w$  correspond to their respective cartesian x, y, and z velocities ( $\text{m.s}^{-1}$ ),  $t$  corresponds to time (s), and material derivative is defined as  $\frac{D}{Dt} = \frac{\partial}{\partial t} + u \frac{\partial}{\partial x} + v \frac{\partial}{\partial y} + w \frac{\partial}{\partial z}$ . Furthermore,  $\rho$  corresponds to the gas density ( $\text{kg.m}^{-3}$ ),  $P$  corresponds to the gas pressure (Pa),  $T$  corresponds to the gas temperature (K), and  $\mu$  is the viscosity of air set to  $1.789 \times 10^5 \text{ kg.(m.s)}^{-1}$ . The force component ( $N$ ) in the  $i$ th direction is denoted by  $F_i$ , such as the forces derived from gas-powder interactions. Due to the supersonic nature of the gas flow, a high Reynolds number is expected. Therefore, gas turbulence was calculated using the realizable  $k-\epsilon$  model outlined in Refs [28, 29].

$$F_d = \exp \left( - \left( \frac{d}{\bar{d}} \right)^n \right) \quad (6)$$

The Lagrangian (i.e., discrete) phase incorporates the Discrete Phase Modeling method implemented in ANSYS Fluent. Spherical Cu powders were injected into the flow domain at 0.15 g/s at the nozzle inlet port and have a diameter range  $d$  of 5–44  $\mu\text{m}$  and a  $\bar{d} \approx 36 \mu\text{m}$ , which can be seen from the data in Fig. S1 (Supporting Information). These radius dimensions were translated into the Rosin-Rammler model [30] shown in Eq. (6) to accurately simulate the powder diameter distribution, with the # of diameters set to 10 and the spread parameter  $n$  set to 3.5. Furthermore, the powders are injected radially along the powder inlet port at 10 m/s, and it is assumed that there is no inlet trajectory variation resulting from powders rebounding within the powder feed tube. This way, the powder trajectories stay parallel to the feed tube section of the model. Notably, for discrete phase modeling, it is assumed that powder-powder collisions are infrequent and can therefore be ignored in the modeling [28].

The force equation used to describe the powder flow is outlined in Eq. (7) [28]:

$$m_p \frac{d\vec{v}_p}{dt} = C_D \rho (\vec{v} - \vec{v}_p) |\vec{v} - \vec{v}_p| \frac{A_p}{2} + \vec{g} \left( \frac{\rho_p - \rho}{\rho_p} \right) + \vec{F} \quad (7)$$

In this equation,  $A_p$  is the powder's cross-sectional area ( $\text{m}^2$ ),  $m_p$  is the Cu powder's mass (kg),  $\vec{v}_p$  and  $\vec{v}$  are the powder and gas velocity vectors ( $\text{m.s}^{-1}$ ), respectively, and  $\rho_p$  and  $\rho$  are the powder and gas densities, respectively. Additionally,  $\vec{g}$  is the acceleration of gravity in vector form, which is  $-9.81 \text{ m.s}^{-2}$  in the y direction. The drag coefficient  $C_D$  corresponds to the drag of the spherical Cu powders, modeled as

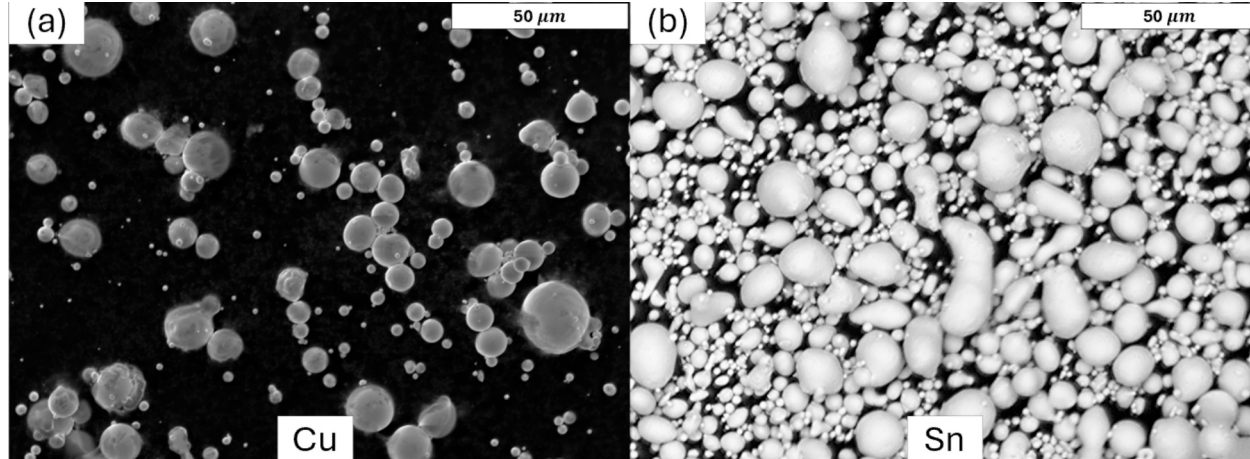


Fig. 2. Morphologies of (a) copper (Cu) and (b) tin (Sn) feedstock powders.

$C_D = a_1 + \frac{a_2}{Re} + \frac{a_3}{Re^2}$ , which was initially derived from Morsi and Alexander [31] with constants  $a_1$ ,  $a_2$ , and  $a_3$ . A high Mach number flow correction assumption was also incorporated for flows where  $M_p > 0.4$  and particle Reynolds Number  $Re_p > 20$  [32]. It is important to note that the effects of powder rotation were not considered during the modeling analysis.

The force term  $\vec{F}$  corresponds to additional external forces experienced by the powders, which in this case mainly involves the two-way transfer of momentum between the turbulent gas and discrete particle phases, which is described in Eq. (8) [28]:

$$F_p = \sum \left( \frac{18\mu C_D Re}{\rho_p d_p^2 24} (\nu_p - \nu) + F_{other} \right) \dot{m}_p \Delta t \quad (8)$$

The particle transfer force  $F_p$  is mainly affected by the first gas flow term, where  $Re$  is the flow Reynolds Number,  $d_p$  is the particle diameter,  $\dot{m}_p$  is the particle mass flow rate, and  $\Delta t$  is the flow time step.  $F_{other}$  describes any additional force input terms encountered in the modeling of the gas-powder flow.

A free-stream 3D domain was constructed based on the nozzle geometry outlined in Fig. 3a. It is important to note that the radial injection port supplying powder to the nozzle necessitates the use of a 3D model due to the non-axisymmetric powder flow. The flow domain consists of the main pressurized gas inlet port, the powder inlet port, and ambient inlet surfaces. The ambient inlets and outlets are set on the faces of a 25 mm × 40 mm cylinder, with the outlet set to the forward cylinder face and the inlets set to the side and rear faces. An 8 mm × 5 mm cylindrical pocket is cut away from the rear cylinder face and is connected to the CS nozzle exit port, such that the nozzle exit is 35 mm away from the outlet face. Overall, the entire mesh comprises a total of 3,053,505 elements, which is greater than the highest number of elements in the

mesh convergence study outlined in Ref [27] that incorporates a nearly identical flow domain model but focusing on a steady-state flow. Additionally, the area-weighted average of the nozzle wall  $y^+$  values at  $t = 100$  ms were calculated to be around 33, which is suitable for turbulent-dominant flow domains [33].

To approximate the pressure control of the solenoid valve, the gas inlet port was prescribed a time-dependent pressure function with a maximum gauge value of 0.7 MPa and a total cycle time of 200 ms, which is outlined in Eq. (9):

$$P = 0.7[\text{MPa}] \left( \frac{1}{1 + e^{-300(t-0.025)}} - \frac{1}{1 + e^{-300(t-0.175)}} \right) \quad (9)$$

The overall shape of the pressure function is outlined in Fig. 4a. When analyzing the inlet pressure function, the pressure reaches 81 % of the maximum pressure at 30 ms and 170 ms, and 99 % of the maximum pressure at 50 ms and 150 ms. Furthermore, the powder inlet and ambient inlets/outlets are all set to atmospheric pressure. A coupled pressure-velocity scheme with a least squares cell based spatial gradient discretization model was implemented using second order upwind formulations for all aspects of the Eulerian phase. To compute the transient model, a time step of  $5 \times 10^{-5}$  (s) was used and computed using a first order implicit scheme.

#### 2.4. Particle image velocimetry (PIV)

The PIV method was used to validate the CFD model, with the experimental shown in Fig. 4a. The PIV equipment and analysis software used here are similar to those described in [34]. To elaborate, two laser sheet pulses from a dual-head, Nd:YAG laser (532 nm wavelength, maximum energy of 200 mJ per pulse, 5 ns pulse length, Quantel

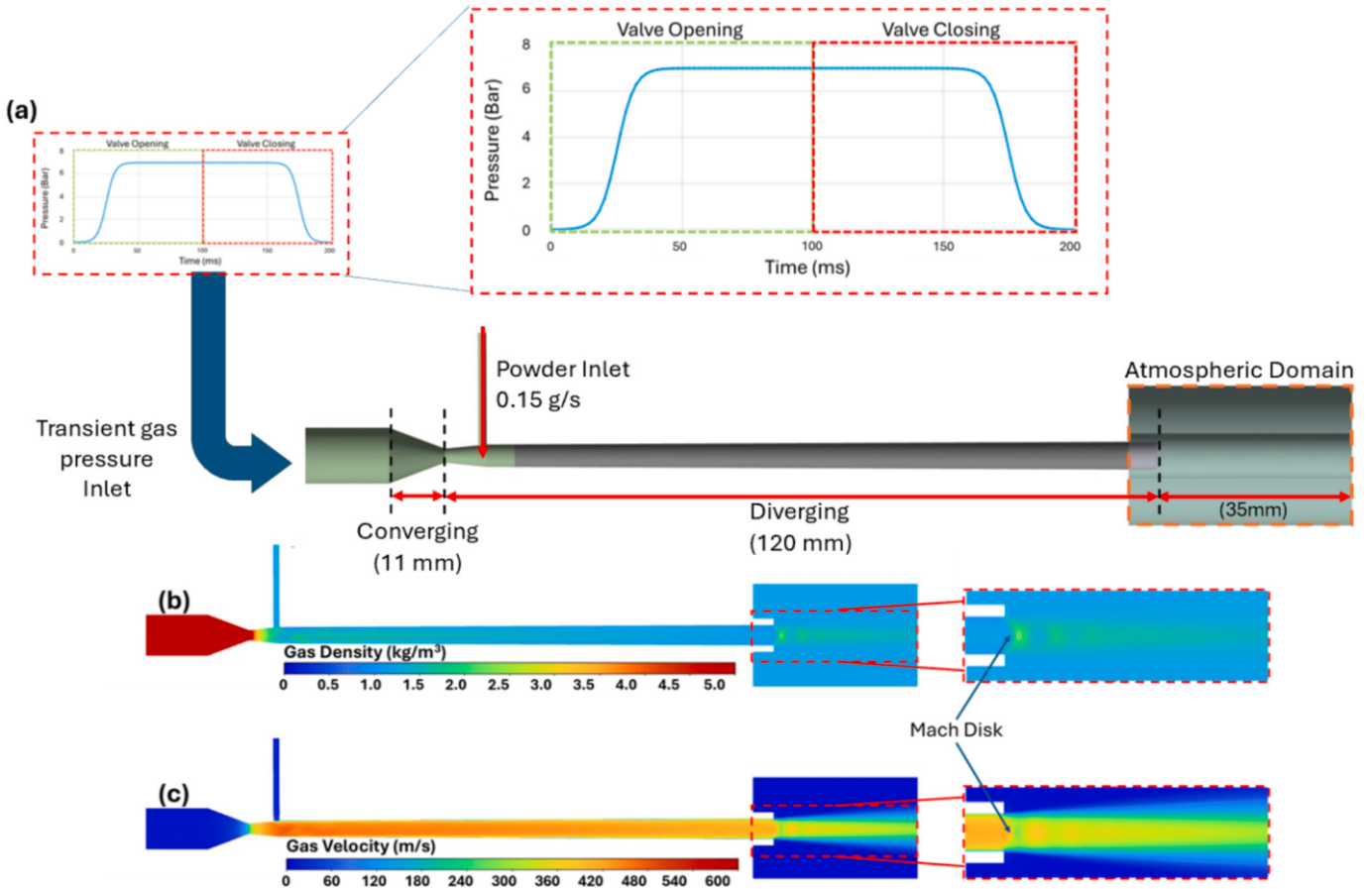


Fig. 3. (a) Modeling domain overview, including the pressure inlet pulse function; (b) gas density; (c) gas velocity distribution within the PCS system at fully developed flow stage.

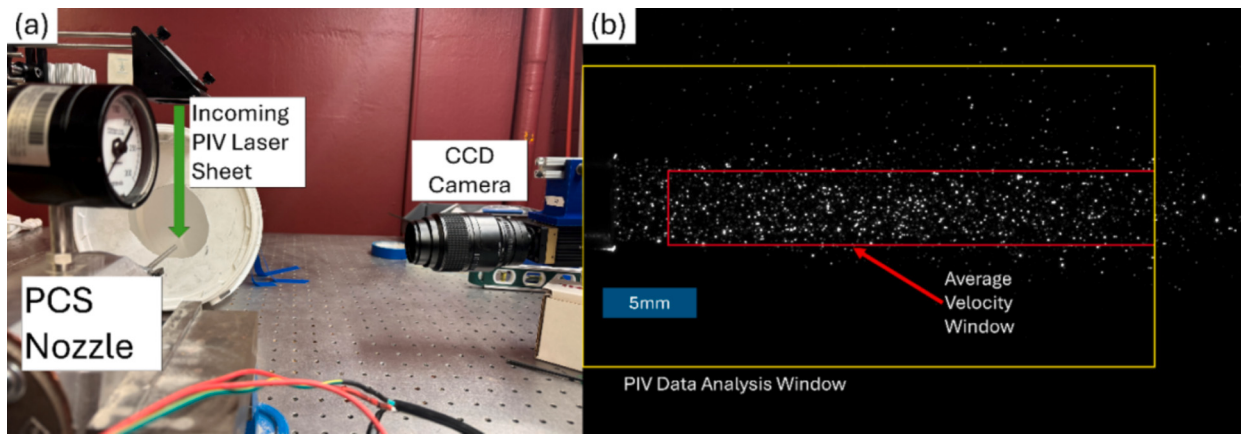


Fig. 4. (a) PIV setup (b) a CCD camera image captured via PIV analysis.

*EverGreen*) are used to illuminate the powders in-flight, with a 510 ns delay between pulses. This delay is captured by a 2752 × 2208 pixel charge-coupled device (CCD) (*Bobcat B2720*) positioned normal to the laser sheet, employing a double exposure capture method to obtain an image pair.

A signal output from the PIV controller controls both the PIV laser pulses and the solenoid valve of the PCS nozzle. The solenoid valve of the PCS nozzle was programmed with a 200 ms delay between the open

and close commands. Meanwhile, to account for the delays of the circuitry, a 100–400 ms delay was introduced between the PCS actuation signal and the PIV capture signal. It is assumed that the valve is fully open by 100 ms, and fully closed by 300 ms. Within the 100–300 ms timeframe, intervals of 25 ms were used, with each interval corresponding to 5–10 PIV image pairs captured for data analysis. Two additional time markers at 350 ms and 400 ms were also captured to determine powder flow after valve closure. Considering these delays, the

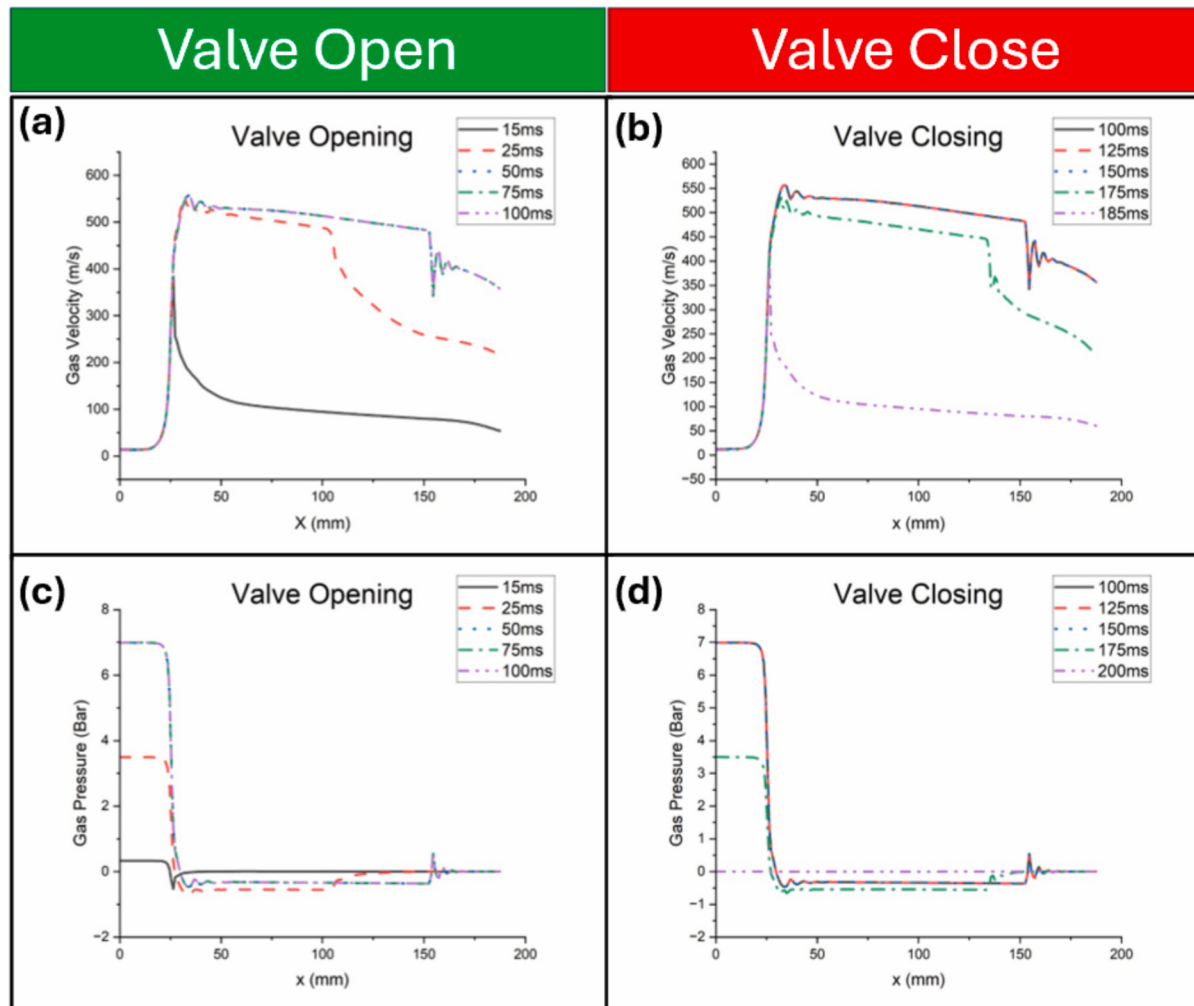


Fig. 5. Gas velocity (a-b) and gas pressure (c-d) along the nozzle centerline at different stages of the valve opening and closing cycle.

collected data is presumed to capture powder velocity development from 0 to 300 ms, with the solenoid valve remaining open from 0 to 200 ms.

Fig. 4b shows a CCD camera image capturing the power stream analyzed by PIV analysis. To determine the powder velocity field for each data set, a specific region was selected that fully encompasses the visible powder spray (see yellow region in Fig. 4b). This region underwent post-processing by a PIV analysis software (*Davis 8.4*) using a multi-pass cross-correlation algorithm. The first iteration uses  $64 \times 64$  pixel windows with a 50 % overlap for 5 passes. Subsequently,  $32 \times 32$  pixel windows with a 50 % overlap were used to refine the data from the first iteration, with an additional 5 passes. This 50 % overlap results in a corresponding vector resolution of 16 pixels (0.346 mm). Following data analysis, outlier velocity values ( $\leq 200 \text{ m/s}$ ) were culled from the data, and the average powder velocity was calculated within a  $5 \text{ mm} \times 30 \text{ mm}$  window.

### 3. Results and discussions

#### 3.1. Gas flow analysis

The transient nature of the nozzle flow is crucial for determining the timing of the PCS device operation, particularly to establish how long the gas flow develops during each pulse cycle. Additionally, it is important to understand the type of supersonic nozzle flow the PCS nozzle produces, as normal shock waves have been shown to reduce powder velocities for the CS process. The development of gas velocity and gas pressure over time is illustrated in Fig. 5, showing the gas velocity during the valve opening and valve closing phases, respectively. The first 100 ms corresponds to the valve opening, and the second 100 ms corresponds to the valve closing. By 25 ms, the CD nozzle flow reached a supersonic state, with a normal shock wave forming inside the nozzle. This indicates a sharp drop in gas velocity and a sharp increase in gas pressure at 100 mm from the nozzle. Additionally, as time progresses, the high gas speed causes pressure drop below atmospheric levels after the nozzle throat, then rise back to atmospheric pressure after the normal shock wave. This phenomenon can be seen from 75 ms–125 ms at the 25 mm and 155 mm markers, respectively, in Fig. 5c-d.

From  $t = 50 \text{ ms}$  to  $t = 150 \text{ ms}$ , the gas flow is fully developed and corresponds to the steady-state condition, as demonstrated by overlapping gas velocity and pressures in Fig. 5 at the 50, 100, and 150 ms intervals. The ripples in the graphs after the 150 mm location correspond to Mach diamonds formed at the end of the nozzle. By 175 ms, the gas flow recedes again, but unlike the 50 ms interval, a small ripple effect (i.e., propagation of waves through a gas medium) corresponds to a smaller set of Mach diamonds that dissipate as the shock wave recedes. Importantly, the exiting gas velocity at the end of the domain (standoff distance of 35 mm) drastically drops off when the gas flow is not fully developed, with a difference of 145–150 m/s between  $t = 50 \text{ ms}$  and  $t = 75 \text{ ms}$ , as well as between  $t = 125 \text{ ms}$  and  $t = 150 \text{ ms}$ . As such, only the time when Mach diamonds formed after the nozzle tip should be considered as vital to the pulse cycle.

To better understand when Mach diamonds form at the nozzle tip, more granular intervals of 10 ms are needed. As seen from Fig. 6, gas velocity crosses the  $M = 1$  threshold around the 20 ms mark, where the gas velocity rapidly increases. At 20 ms, a prominent normal shock wave formed right before the powder inlet port location. From this point, it takes about 10 ms for the normal shock wave to travel through the nozzle to its exit, where Mach diamonds form at 30 ms. At this stage, the gas velocity at a standoff distance of 35 mm from the nozzle tip has reached around 308 m/s, which is 48 m/s lower than the gas velocity at 50 ms – 356 m/s at 35 mm from the nozzle tip. Further gas development continues for an additional 10 ms, but the gas velocity values at the nozzle tip remain nearly equal in the 40–50 ms range. As shown in Fig. 5, the overall gas velocity and pressure development when the valve closes

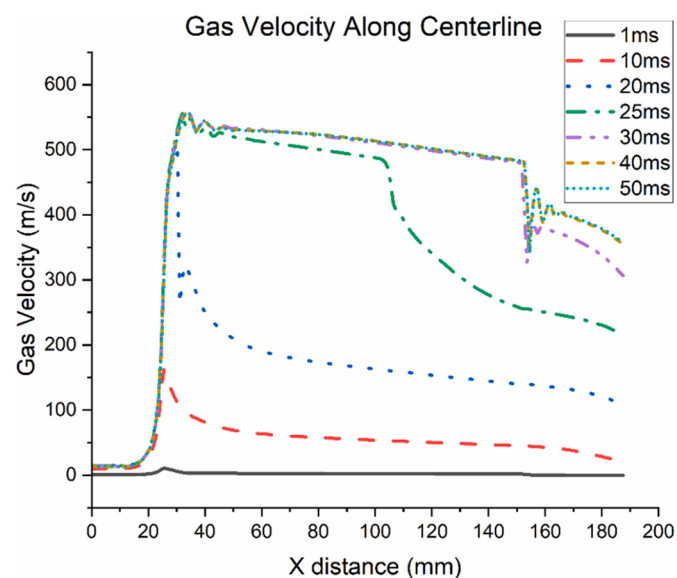


Fig. 6. Gas velocity development during the valve opening phase.

nearly mirrors the gas velocity development when the valve opens. This is due to the symmetric nature of the inlet pressure condition specified in Eq. (9).

A more refined understanding of the shockwave development can be seen in Fig. 7, which illustrates how the normal shock wave travels through the nozzle as pressure rapidly increases. The normal shock wave initially forms from the nozzle throat and travels towards the nozzle's tip. From 15 to 20 ms, the normal shock wave moves forward unperturbed as it approaches the powder inlet port. However, at 20 ms, the lower pressure gas flow stream interacts with the normal shock wave inside the nozzle, resulting in oblique shock waves that reflect along the diverging nozzle walls. This phenomenon corresponds to the oscillations produced in Fig. 6 between the 30 and 50 ms marks and is clearly shown in the 25–35 ms timeframe in Fig. 7. These reflections do not travel the entirety of the diverging section; a normal shockwave forms after the reflections dissipate, as seen at 25 ms. By 30 ms, shock wave has exited the nozzle, and a Mach disk formed. Finally, by 35 ms, the gas flow has fully developed, with Mach diamonds forming in the nozzle's jet, indicating a steady state solution. This is evident when comparing Figs. 4b-c to 7, showing that the gas flow at 100 ms is practically identical to the gas flow at 35 ms.

This flow pattern forming a Mach disk corresponds to an increase in pressure seen in Fig. 5 from inside the nozzle to the ambient pressure, showing that the nozzle's flow is overexpanded. Due to the gas pressure being below atmospheric pressure inside the nozzle's converging section, a vacuum effect is induced from the powder inlet port, which feeds powder at ambient pressure. However, in cases of overexpanded flow, the Mach disk results in a significant drop in gas velocity, caused by a normal shock forming from an oblique Mach at the nozzle's tip. In this case, the gas velocity decreases from 480 m/s at the nozzle tip to around 400 m/s once the Mach diamonds have dissipated.

Such strong shock waves, including normal and bow shocks, have been shown to affect powder velocity of small diameter particles [35–37], thereby limiting overall powder velocity early in the nozzle's exiting jet. Fig. 4c highlights a notable decrease in gas velocity along the diverging section of the nozzle, which can be seen in Figs. 5–6. A peak velocity of 556 m/s is reached inside the nozzle, gradually decrease from 530 to 525 m/s at around 53–73 mm along the length of the nozzle.

Finally, the development of gas flow as the valve closes mirrors that of the valve opening case as shown in Fig. 7. As time progresses from 165 ms to 170 ms, the intensity of Mach diamonds begins to diminish, resulting in similar gas velocities by 175 ms. Unlike the valve opening

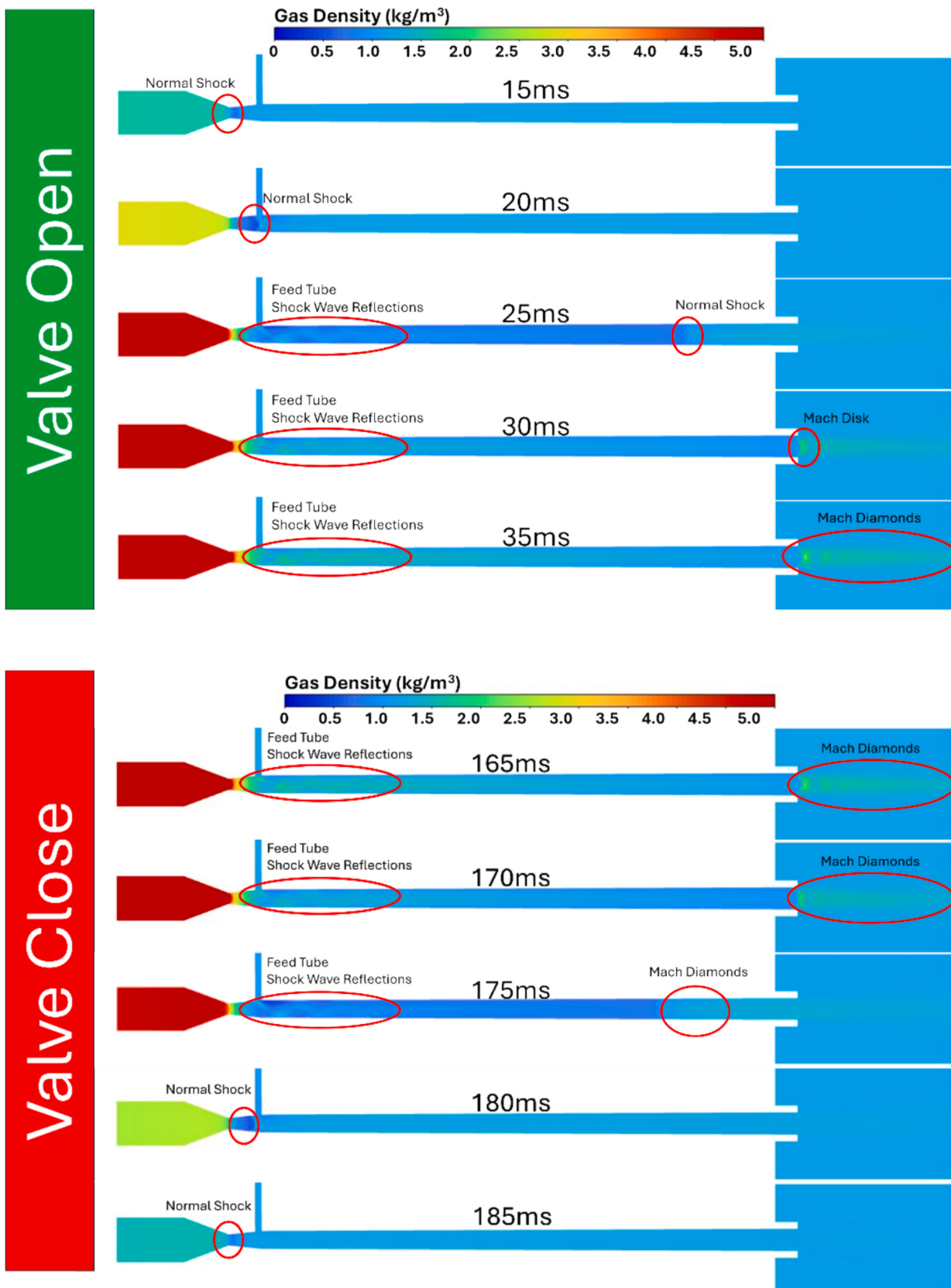


Fig. 7. Shock wave formations during the valve opening (upper panel) and valve closing (lower panel) phases.

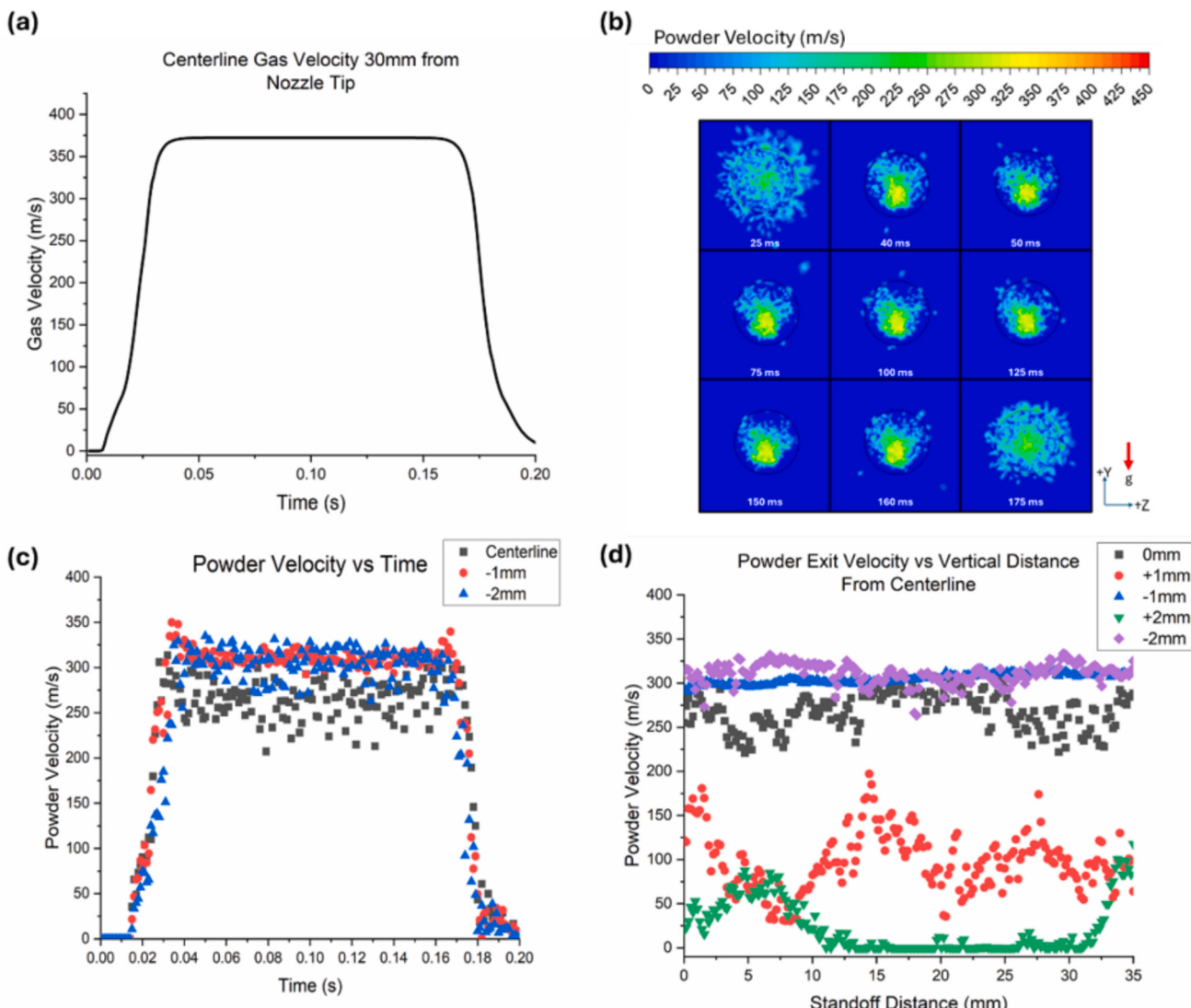
case, Mach diamonds persist inside the nozzle at 175 ms, indicating that is more favorable for the gas flow to separate from the nozzle walls as the shock wave formation travels towards the nozzle throat. However, the presence of the shockwave reflections from the feed tube dissipates the Mach diamonds, resulting in a similar normal shock formation at 180 ms, resembling the flow state observed at is 20 ms.

### 3.2. Powder flow analysis

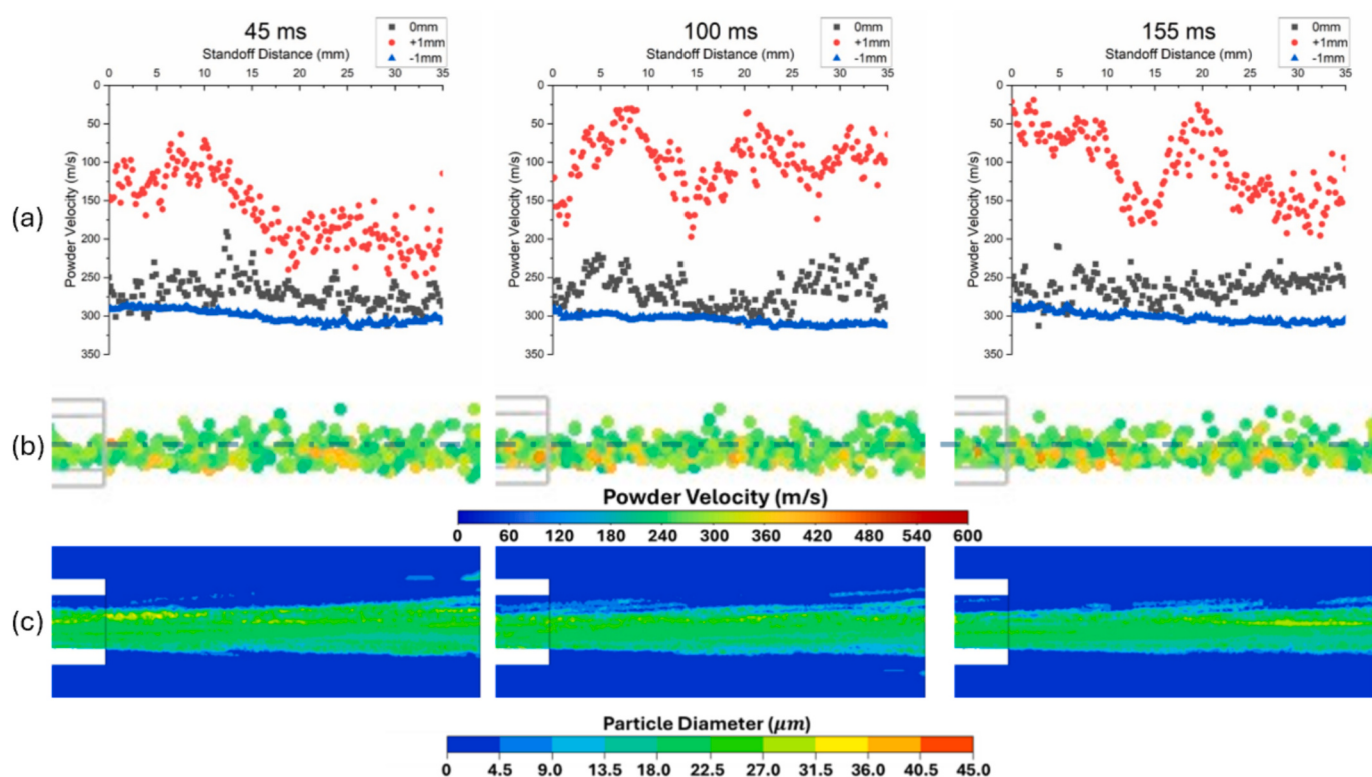
A full transient analysis of the free-stream powder velocity in comparison the transient development of the free-stream gas velocity is shown in Fig. 8a-d. By examining the transient analysis of powder flow development over time, it is evident that the timing of acceleration and deceleration of powder flow at the end of the free stream jet closely matches that of the gas flow at the same point, as shown in Fig. 8a and c. The majority of the acceleration occurs at 15–35 ms and 165–185 ms time markers, which corresponds to the travel of the normal shock wave from the powder inlet port to the nozzle outlet (see Fig. 7). However, unlike the radially symmetrical gas velocity, powder velocity is notably affected by gravitational acceleration. In this case, the powder fully developed powder velocity is highest at around 1–2 mm below the nozzle tip and decreases at and above the nozzle's centerline (see

Fig. 8b-d). Notably, this change in powder concentration and velocity is time dependent, with powders clustering together from 50 ms to 150 ms, as seen in Fig. 8b.

This phenomenon is best seen when analyzing the powder velocity at, above, and below the powder stream when the gas flow is considered fully developed, which occurs between 45 and 155 ms. Fig. 9a-b compares the velocity development of the free stream powders during the 45, 100, and 155 ms time markers, indicating the bounds of steady-state flow. Meanwhile, Fig. 9c shows the powder size distribution contour in the free stream jet. In all three cases, powder velocity magnitude increases in the -y direction, corresponding to the concentration of higher velocity particles below the nozzle centerline. However, the largest variation in powder velocity seen in Fig. 9a is most notable at the 100 ms time point, where powder concentration is heavily favored below the nozzle's centerline at this point, whereas powders are more evenly distributed at 45 and 155 ms along the vertical direction, as seen in Fig. 9b-c. However, powders at or above the centerline are slower than those below the centerline. This can be seen when comparing the powder velocity values to the particle diameter concentrations in the jet; the larger and therefore heavier powders are concentrated at and above the nozzle centerline, whereas smaller and therefore lighter powders are concentrated below the centerline, as seen in Fig. 9c. Additionally, many



**Fig. 8.** (a) Gas velocity at the centerline to powder velocity development; (b) the powder velocity development 30 mm from the nozzle tip; (c) particle velocity versus time along the centerline, and radial offset with 1 and 2 mm; (d) steady-state particle velocity at various nozzle standoff distances.



**Fig. 9.** Time-based comparison between (a) average particle velocity values between  $-1$  to  $1$  mm around the nozzle centerline vs nozzle standoff distance, (b) powders trajectory colored by their velocity value and (c) powder diameter concentration of the powder jet.

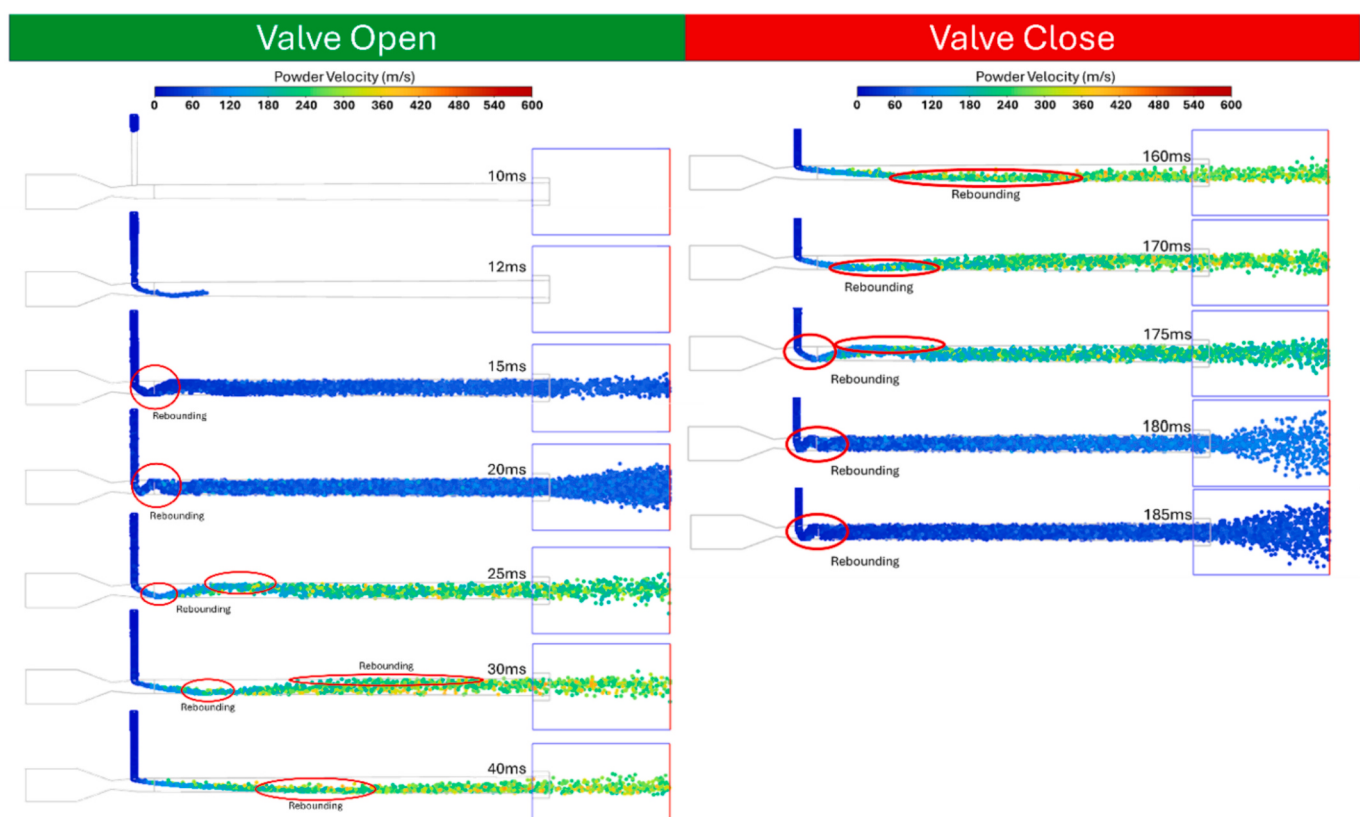


**Fig. 10.** Powder flow development during the 10–70 ms timeframe of the valve opening stage.

of the smallest particles are concentrated several millimeters above the nozzle centerline.

To better understand this behavior, it is essential to consider the development of the gas-powder flow within the nozzle. Both the gas flow development and powder-wall interactions affect the powder distribution of the exiting powder spray alongside the effects of gravity. Fig. 10 illustrates the powder velocity development over time through particle tracking for both the valve opening and closing phases, including highlighting regions where powders rebound off the nozzle walls. Furthermore, the relevant CCD images for this time frame are provided in Fig. S2 (Supporting Information). The initial development of the gas-powder flow begins at around 12 ms, where the pressure at the powder injection point is below atmospheric pressure and therefore powder flow is induced via a vacuum effect. These initial powders reach the 35 mm standoff distance marker at the end of the domain by 15 ms, where the powder stream begins to increase in velocity over time. Notably, by 15–20 ms powders are seen to be rebounding against the nozzle wall and dispersing throughout the nozzle at a steady pace. As the gas velocity increases, specific rebounding spots are observed within the nozzle, with 1 significant location at 20 ms and 2 significant locations at 25 ms not too far after the nozzle throat. At this point, the impact angle onto the side wall has increased significantly, as the normal shock wave seen in Fig. 7 has progressed inside the nozzle, exiting the nozzle at 30 ms. From 30 ms onward, however, the rebounding locations begin to move further up the nozzle as gas velocity rapidly increases. Additionally, these zones begin to spread out within the nozzle, resulting in powders interacting with a larger surface area within the diverging section of the nozzle. Furthermore, the exiting powder jet stream narrows significantly as powders begin to rebound less within the nozzle and are picked up the supersonic gas jet. By 35 ms, the secondary rebounding zone is mostly gone, as powder trajectories are now pointing out towards the nozzle exit and are quickly accelerated by supersonic gas.

However, even though the gas jet has developed by 45 ms, the powder flow continues to change within the nozzle. Fig. 11 plots the powder's axial velocity vs time and compares it to the powder velocity tracking at the 45, 100, and 155 ms intervals. It is possible to identify the regions within the nozzle where the powder is rebounding off the nozzle walls, which corresponds to local minimums in the particle axial velocity value along the nozzle centerline. At  $t = 45$  ms, the particles rebound off the lower diverging wall between 80 and 100 mm from the nozzle inlet, yet by time the pulse cycle is 50 % complete ( $t = 100$  ms), the powders are rebounding between the 90 mm and 120 mm region. This shift of the rebounding region as well as its lengthening is likely due to a slight increase in nozzle inlet pressure and the resulting nozzle gas velocity from  $t = 45$  ms to  $t = 100$  ms. The input pressure function for the main gas inlet measures a gas velocity at  $t = 45$  ms is calculated to be 6.83 bar, whereas at  $t = 100$  ms the gas velocity is calculated to be at 6.99 bar. Although the difference between the gas velocity inside the nozzle is minor, it does show a notable difference of 4.5 m/s at the far end of the gas jet between the two time points. A similar decrease is observed when moving from  $t = 100$  ms to  $t = 155$  ms, corresponding to a backwards shift in the rebounding zone of the nozzle.

Therefore, although the main characteristics of the gas flow are fully developed, slight changes in the nozzle inlet pressure greatly affect the powder flow characteristics. At 45 and 155 ms, the powders rebounding against the nozzle wall enter at a slightly higher angle than the 100 ms time point, and therefore carry a higher radial velocity value both before and after the rebound. Additionally, as the rebounding zone is closer to the nozzle throat, the powders are able to travel for a longer period of time with a vertical velocity component, allowing them to appear above the nozzle centerline in Fig. 9. Meanwhile, at  $t = 100$  ms, the powders have a lower rebounding angle, and thus more horizontal momentum is preserved. As seen in Fig. 9c, the average powder diameter at and above the centerline is higher than the average powder diameter below the

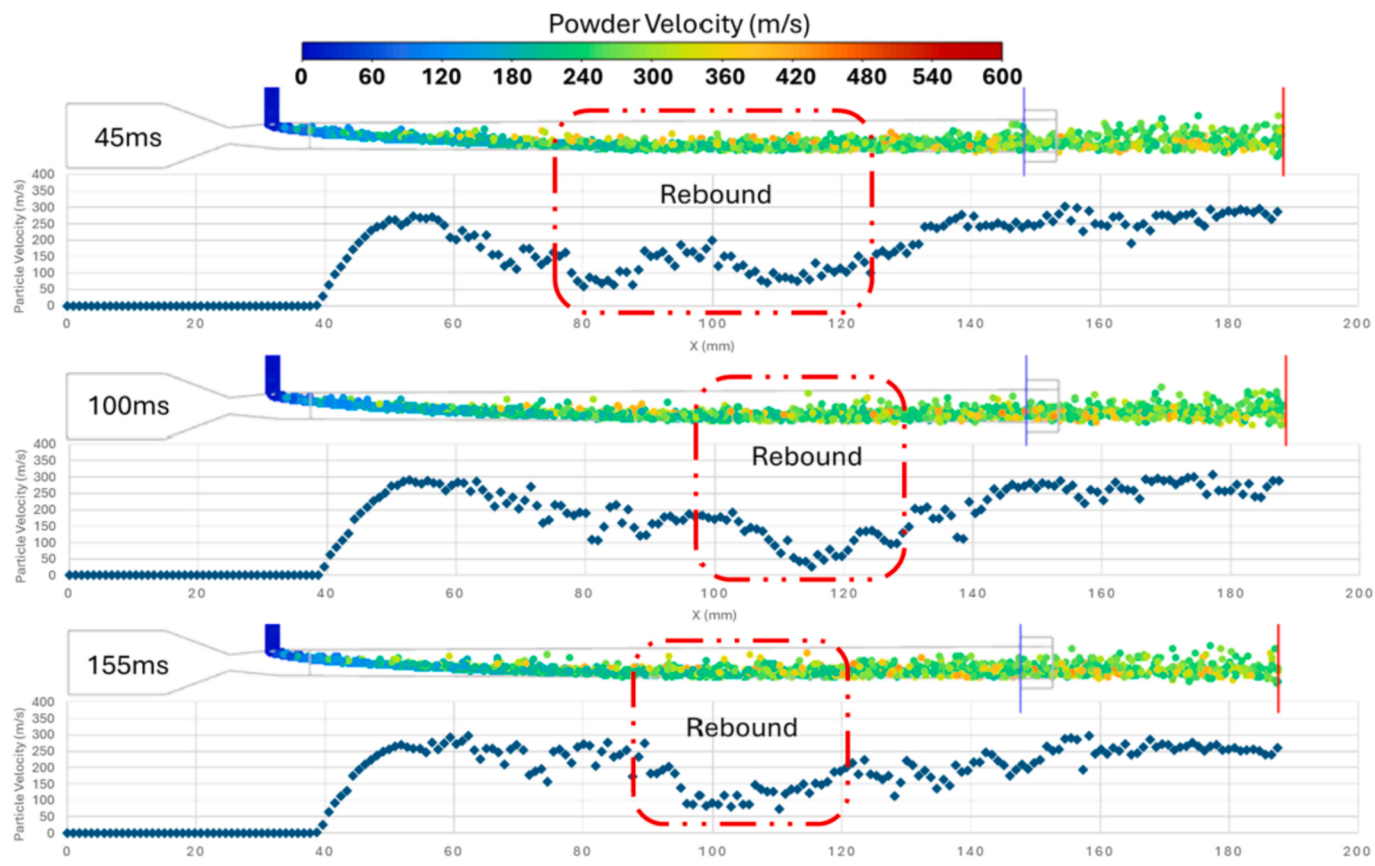


Fig. 11. Powder velocity analysis within the nozzle at  $t = 45, 100$ , and  $155$  ms.

nozzle centerline, especially for the  $t = 45$  and  $155$  ms cases. In this case, heavier powders are less responsive to the influence of the gas flow and are more likely to preserve the radial component of their trajectory due to their higher inertia, while the smaller and lighter powders are more dominated by the axial velocity component as they are more responsive to the acceleration provided by the gas flow. As such, the rebounding of powders results in a distribution such that the powders at or above the nozzle centerline are slightly larger than the powders below the nozzle centerline.

This rebounding behavior of the particles is best corroborated when analyzing the Stokes Number of the powders, which is a nondimensional number determining how easily a given gas flow dictates particle trajectories. The Stokes number equation is as follows [28]:

$$Stk = \frac{\rho_p d_p^2 u_0}{18\mu_g l_0} \quad (10)$$

where  $\rho_p$  is the particle density ( $8978 \text{ k.m}^{-3}$ ),  $d_p$  is the particle diameter,  $u_0$  is the gas flow velocity,  $\mu_g$  is the gas viscosity ( $1.789 \times 10^{-5} \text{ kg.(ms)}^{-1}$ ), and  $l_0$  is the characteristic length, which is the nozzle exit diameter of  $5 \text{ mm}$ . It is important to note that a high Stokes number ( $Stk \gg 1$ ) indicates the powders are dominated by their momentum, whereas a low Stokes number ( $Stk < 1$ ) indicates that the gas flow dominates the powders' trajectory. By taking the smallest powder diameter of  $5 \mu\text{m}$ , we can determine the minimum Stokes number range of powders based on the gas velocity values seen in Figs. 5–6. Notably, the  $5 \mu\text{m}$  diameter particles have a Stokes number range of  $69.7$ – $76.7$  inside the nozzle, and  $48.9$ – $55.8$  outside the nozzle during steady-state flow. This shows that all powders are momentum dominated during the steady-state flow phase of the PCS pulse, and therefore any amount of powder dispersion is attributed to trajectory from powder rebounding along the nozzle walls. The effect of the final stages of the powder flow development can be observed in Fig. 10 during the valve closing phase. As the gas pressure rapidly decreases, the powder rebounding regions move upstream towards the powder inlet port, eventually culminating in low velocity powders rebounding multiple times within the nozzle before they exit. Furthermore, as also seen in Fig. 10, powders begin to spread out from the nozzle stream, resulting in a large, slow moving cone of powders exiting the nozzle into the open domain. This steady stream of powder flow is induced by both negative pressure at the powder inlet port as well as gravity, resulting in more powders exiting the nozzle. This dispersion can also be checked by an analysis of the Stokes Number, as the centerline gas velocity at  $t = 185 \text{ ms}$  at the nozzle exit is  $80 \text{ m/s}$ . This correlates to a Stokes Number of  $11.2$  for the  $5 \mu\text{m}$  powder diameter, and a Stokes Number of  $903.3$  for the  $45 \mu\text{m}$  powder diameter, showing that the powder flow continues to be dominated by their momentum. As such, this dispersion can be largely attributed to the powders retaining a large amount of their off-axis velocity gained initially from the off-axis powder inlet port. This results in a high rebounding angle inside the nozzle walls, and this non-axial velocity component is easily retained as the powders exit the nozzle, resulting in a large amount of powder dispersion.

From the powder flow analysis, it is apparent that a large portion of the valve opening and closing cycle for the PCS nozzle is unable to accelerate powder velocities to acceptable levels, and therefore would be wasted during the deposition phase and lowering the deposition efficiency of the nozzle. To counteract this, a powder feed control valve should be implemented into the future prototype design. From this analysis, the optimal powder injection time for a  $200 \text{ ms}$  pulse cycle should be at around  $50 \text{ ms}$  and should stop at the  $150 \text{ ms}$  mark, which is when the gas inlet is at  $99$ – $100 \%$  of its maximum pressure. Additionally, increasing the time between the valve opening and closing phases will increase the amount of powder that can be deposited with a well-developed gas flow, though this timing must take into consideration the application requirements. Furthermore, increasing powder velocity and temperature by increasing the nozzle inlet pressure and temperature

can improve this timing window by increasing the maximum particle velocity, and should be considered in future developments to ensure the supplied powders can reach the necessary material-dependent critical velocity.

### 3.3. Model validation

Using the PIV analysis method described in Section 2.3, the velocity vector data was obtained and compared to the CCD camera image as well as the CFD modeling. Fig. 12 shows this validation, with Fig. 12a showing the free-stream powder velocity field, while Fig. 12b shows the CFD particle tracking data with their own velocity magnitudes. Fig. 12c is a CCD image of the free stream particle velocities. When comparing the powder flow velocity field obtained from the PIV during steady-state conditions and comparing it to the corresponding CFD velocity distribution, it is apparent that the Cu powders are accelerated to around the same velocity range of  $250$ – $450 \text{ m/s}$ . This can be best seen when comparing the average of the CFD and PIV velocities during the established steady-state time range of  $50$ – $150 \text{ ms}$ . The average velocities between both the experimental and simulated powder flows show a high agreeability, with a maximum of an  $8.05 \%$  error rate between the PIV and CFD results, which is shown in Fig. 12d. Additionally, the averages of the CFD velocities fall within the standard deviation of the PIV results, and vice versa.

However, the powder distribution of the CFD model does not fully match what is seen in the experimental results. In the CFD model (Fig. 12b), the powders are clustered below the nozzle's centerline due to the effects of gravity, which is not seen in both the PIV powder velocity contour and the CCD camera image (Fig. 12a-c). This wider dispersion seen in the experimental powder flow results is likely due to a difference in powder inlet velocity conditions, as the initial powder trajectories that enter the nozzle will not be completely parallel to the nozzle inlet port. Incorporating a non-parallel initial powder velocity trajectory into the cold spray simulations has been shown to result in higher powder dispersion within the nozzle [27]. Additionally, the CFD scheme's reliance on RANS-based approach limits the observable effects for turbulence-driven dispersion. A more robust model – such as Direct Navier Stokes (DNS) combined with powder rotation- can effectively capture the Magnus effects induced by turbulent eddies [38]. A recent modeling work performed by Raoelison et al. [39] indicates that turbulent flow deformation occurs within the nozzle wall, suggesting that the induced Magnus force may serve as an additional mechanism for powder dispersion inside the nozzle. Besides, incorporating the Large Eddy Simulation (LES) model could more accurately capture the interplay of turbulence, powder dispersion, and Magnus force effects. Future investigations of gas-powder flow within the PCS would benefit from these considerations to better explain powder dispersion phenomena.

Finally, Fig. 13 shows the comparison between experimental and simulated powder velocities. When analyzing the average velocity seen from the PIV analysis over time, as seen in Fig. 13a the average powder velocity does show a notable trend over time. From  $0$  to  $50 \text{ ms}$ , the powder quickly reaches the  $240$ – $250 \text{ m/s}$  range. This velocity then increases to the  $275$ – $300 \text{ m/s}$  range, where the powder velocity plateaus from  $50 \text{ ms}$  to  $150 \text{ ms}$ , before decreasing back to the  $240$ – $250 \text{ m/s}$  range as the valve finally closes. However, instead of rapidly slowing down over a few milliseconds as assumed in the CFD model, as seen in Fig. 13b, the powder velocity gradually reduces over time, with the average powder velocity reaching to around  $211 \text{ m/s}$  at  $300 \text{ ms}$ , or  $100 \text{ ms}$  after the nozzle valve closes. This difference is a notable result of the actual nozzle prototype design, as the solenoid valve is located before the expansion chamber within the nozzle. In this case, additional pressurized gas still must exit the expansion chamber through the nozzle, pulling in and ejecting additional powder as the gas pressure inside the expansion chamber slowly returns to atmospheric pressure.

Despite the differences in the starting and ending powder velocity development between the CFD model and the experimental PIV results,

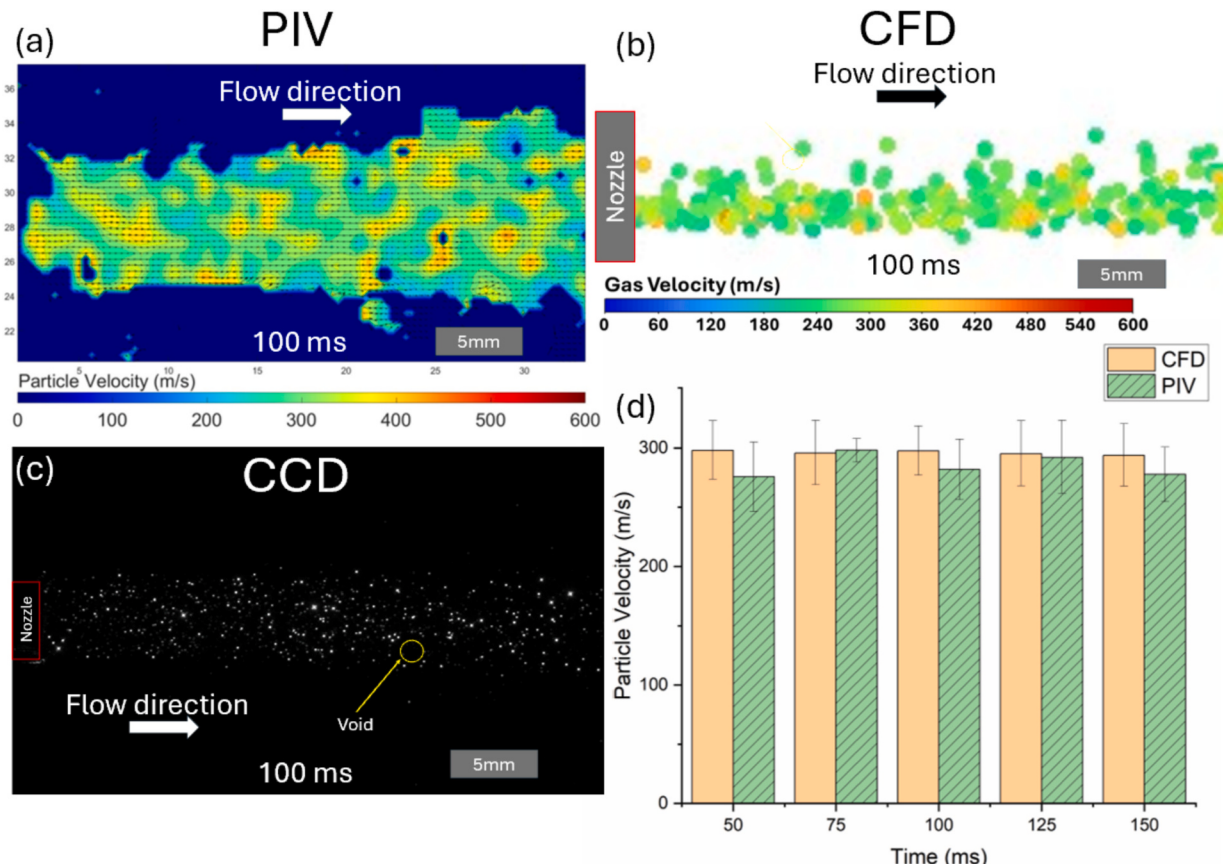


**Fig. 12.** Validation of CFD modeling via PIV at steady-state flow, with (a) PIV powder velocity contour; (b) CFD discrete-phase powder velocity map; (c) CCD image of exiting powder stream; (d) comparison and validation of average powder velocity.

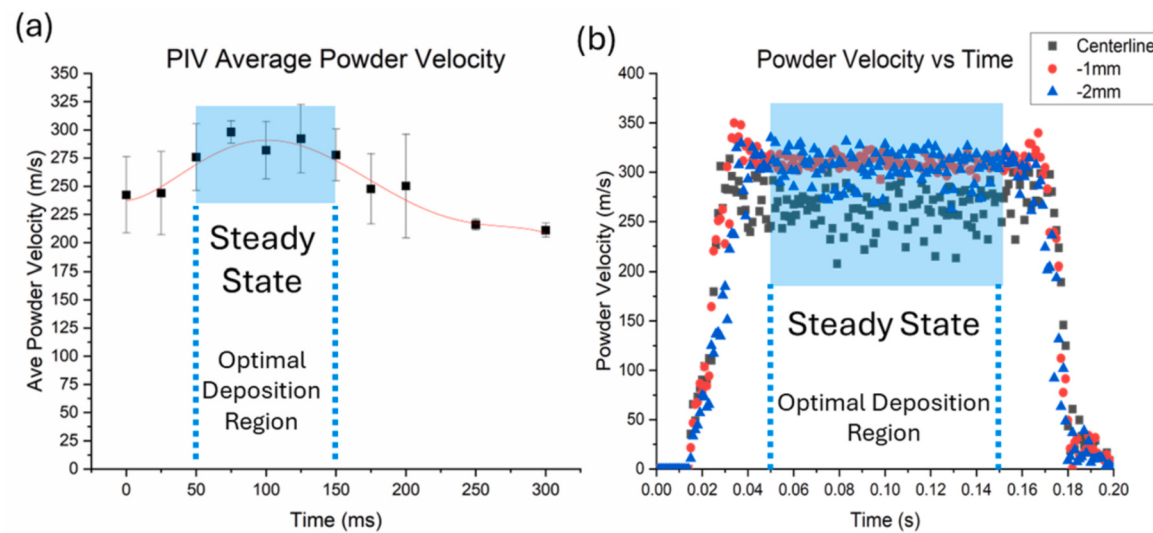


**Fig. 13.** Powder velocity development obtained from (a) PIV data and (b) CFD simulations, with steady-state flow regions.

both analyses confirm that there is at least a 100 ms window of time where the powder velocity has reached steady-state conditions for a single valve open/close pulse cycle of 200 ms. This optimal window is shown in Fig. 13a-b. As such, it is imperative that future developments for the Pulsed CS nozzle incorporate a powder feed control mechanism where powder is timed to be fed only in the allotted 100 ms range. This range, of course, can be increased or decreased depending on the delay allotted for the solenoid valve to open and close. Additionally,

increasing the pressure supplied to the PCS nozzle will increase the overall average powder velocity, allowing for a larger window of time to feed powder during a single pulse cycle. Furthermore, the implementation of a more robust gas-powder control mechanism will eliminate wasted powder and gas exiting the nozzle seen in the experimental validations.

#### 4. Experimental section

From the experimental and simulated characterization of the nozzle, it can be observed that the PCS nozzle is able to accelerate powders up to 300 m/s when supplied with room temperature gas. This velocity value is not well suited for deposition of Cu powders, which have a critical velocity value around 450–500 m/s [40]. However, Sn powders have a much lower critical velocity [38], and therefore can be used to characterize the nozzle's performance at room temperature. Single-pulsed spots of powder were deposited onto PET film, with the nozzle being supplied 7 bar of room temperature air as shown in Fig. S3 (Supporting Information), with standoff distance of the nozzle set at 20, 30, and 40 mm between the nozzle tip and the substrate.

Additionally, the ability of the PCS to deposit metal powders on metal targets was explored. In this regard, Cu particles were deposited onto an 0.635-mm thick Al substrate using the PCS at inlet pressures of 11.4–12.4 bar. Fig. S4 (Supporting Information) illustrates successful Cu deposition on the Al plate, confirming the versatility of the PCS for various powder and substrate materials. In these experiments, the pulse length of the solenoid valve was set to 200 ms, and powder was supplied using a vibratory powder feeder with an oscillation rate of 5 Hz that comes with a standard LPCS system (*Dymet*).

The Sn-PET samples were then examined using a low-magnification microscope as well as an SEM device to characterize the powder deposition. The depositions were then compared to Cold Sprayed (*Dymet*) Sn lines on PET film, where the nozzle travel speed was set to 1800 mm/min, the inlet pressure set to 7 bar (0.7 MPa), the standoff distance to 20 mm, and the gas exit temperature to firstly room temperature (25 °C). The results of the Sn-PET experiments are shown in Fig. 14, where Fig. 14a-b shows the effect of standoff distance on the Sn coating of PET film, whereas Fig. 14c compares the dense PCS-based Sn coatings to the CS-based Sn coatings.

Analyzing the deposited Sn single-pulse samples shows a high dependence of deposition quality on the standoff distance, with a 20 mm standoff distance showing a consistent coated dot measuring between 3 and 4 mm in diameter. As the standoff distance increases, the quality of the deposited spray decreases, with 30 mm pulses producing a mix of 2–3 mm wide full depositions and similarly sized semi-sparse patterns. At 40 mm of standoff distance, the depositions are highly sparse, with some samples only having a handful of visible powder spots.

This discrepancy in the deposition quality is best attributed to a reduction in the amount of powders able to achieve critical velocity as the powders travel further away from the nozzle during steady-state flow. This is best observed when analyzing the powder velocity along the nozzle's centerline, shown in Fig. 8d. In this case, the particle velocity within the powder stream reaches a consistent velocity around 300 m/s at standoff distances between 15 and 25 mm from the nozzle tip. However, the powder velocity at the nozzle centerline begins to drop off, while powders below the centerline retain their velocity. As shown in Fig. 9, the average particle diameter is higher closer to the nozzle centerline and therefore are more affected by drag forces due to the larger particle cross-sectional area. As such, a lower percentage of powders reach critical velocity at higher standoff distances, resulting in a reduction of deposition density and the creation of sparse deposits.

Although high quality depositions are obtained with the closer standoff distances and are the most optimal for typical coating and additive manufacturing applications, the pulsed nozzle system also allows for controlled creation of sparse powder deposits, which could be advantageous in applications, where the stochastic nature of powder sprays is beneficial. As such, it is important to understand the quality of the deposition on the microscale level in comparison to traditional cold spray applications, as the quality of PCS depositions.

Firstly, SEM images were taken of sample deposits made using 20 mm and 30 mm standoff distances, which is shown in Fig. 14a-b. As seen with the 20 mm deposition sample, the coating is shown to be notably dense, with a porosity of only 2.82 %, although there is some porosity

seen throughout the coated sample. Despite these small voids, the powders are well bonded together, with little to no distinction between where one powder begins and another ends. This type of coating suggests that the Sn powders reach well above the critical velocity to not only bond with the PET substrate, but with each other as well. Furthermore, this bonding can be seen even in the more sparse 30 mm standoff distance case, where individual powders are shown to not only be significantly deformed but also cluster and fuse together. In these clusters, it is not fully evident where one powder ends and another begins. As such, the Sn powders that do reach critical velocity to deposit on a sparse pattern are able to fuse well together while also interlocking with the thin PET substrate. In these cases, the PCS prototype demonstrates the ability to create dense and sparse coatings with good adhesion to the substrate and to itself, the former which is valuable for creating functional circuits through cold spray polymer metallization [41].

Fig. 14c shows SEM images of the dense PCS coating at room temperature (RT, 23 °C) in comparison to traditional CS coatings at RT and at 300 °C. When comparing the porosity of PCS to CS at RT, the PCS coating has a denser coating with only 2.82 % porosity compared to the 4.88 % porosity of the CS coating. Although both coatings show substantial fusion between each other, there are more substantial boundaries between powders, and some smaller powders are seen embedded in the Sn coating instead of fused with it when observing the coatings at 1500× magnification. This difference in coating density and is likely due to the differences in the process. Similar observations have been made when comparing coatings made from the PCS process to CS coatings [13]. In the traditional CS system, the nozzle is set to travel along a given path and therefore does not linger in a single location for long. In this case, the nozzle travels along the path at 1800 mm/min, or 30 mm/s; for a given 4 mm square section, the nozzle only covers that region in about 133 ms. Additionally, the entirety of the region is not covered by the nozzle's spray for the whole exposure time, which reduces the number of powders that impinge on that area in a given time. The PCS nozzle, however, will stay at a given location until the cycle is completed, which for this case is set to 200 ms. As such, more powder is deposited onto the substrate, allowing for more powders to fuse together and fill in would-be gaps.

#### 5. Conclusion

In this study, a PCS system using a CD nozzle form factor was designed, prototyped, and characterized. The two-phase gas-powder flow was modeled and characterized in 3D using CFD modeling, followed by experimental validation via PIV. Afterwards, Sn and Cu coatings were deposited on PET film and Al sheets, respectively. The effects of standoff distance and inlet pressure on coating quality were analyzed. Finally, the microstructure of the resulting coatings was examined, with the dense coatings compared to those produced from a conventional CS. The key takeaways from the study are:

- Numerical modeling predicted the PIV-based experimental values (i.e., average powder velocity) within a ≈8 % error rate.
- There is a 100 ms window during which the flow is considered steady-state, making it the optimal time to inject powders into the gas flow. This time period corresponds to when the nozzle inlet pressure is within 99 % of its maximum value.
- The CFD analysis showed that gas-powder flow development closely follows the pressure inlet curve dictated by the action of the solenoid valve, with gas and powder velocity reaching steady state values by 50 ms. Additionally, it takes ~50 ms for gas and powder velocities to return below Mach 0.1 as the valve closes. This suggests that the pressure inlet curve can be used to optimize the powder injection.
- As the inlet valve opens, a normal shock wave moves forward from the nozzle throat to the outlet, leading to the development of Mach diamonds after 35 ms. When the inlet valve closes, these Mach

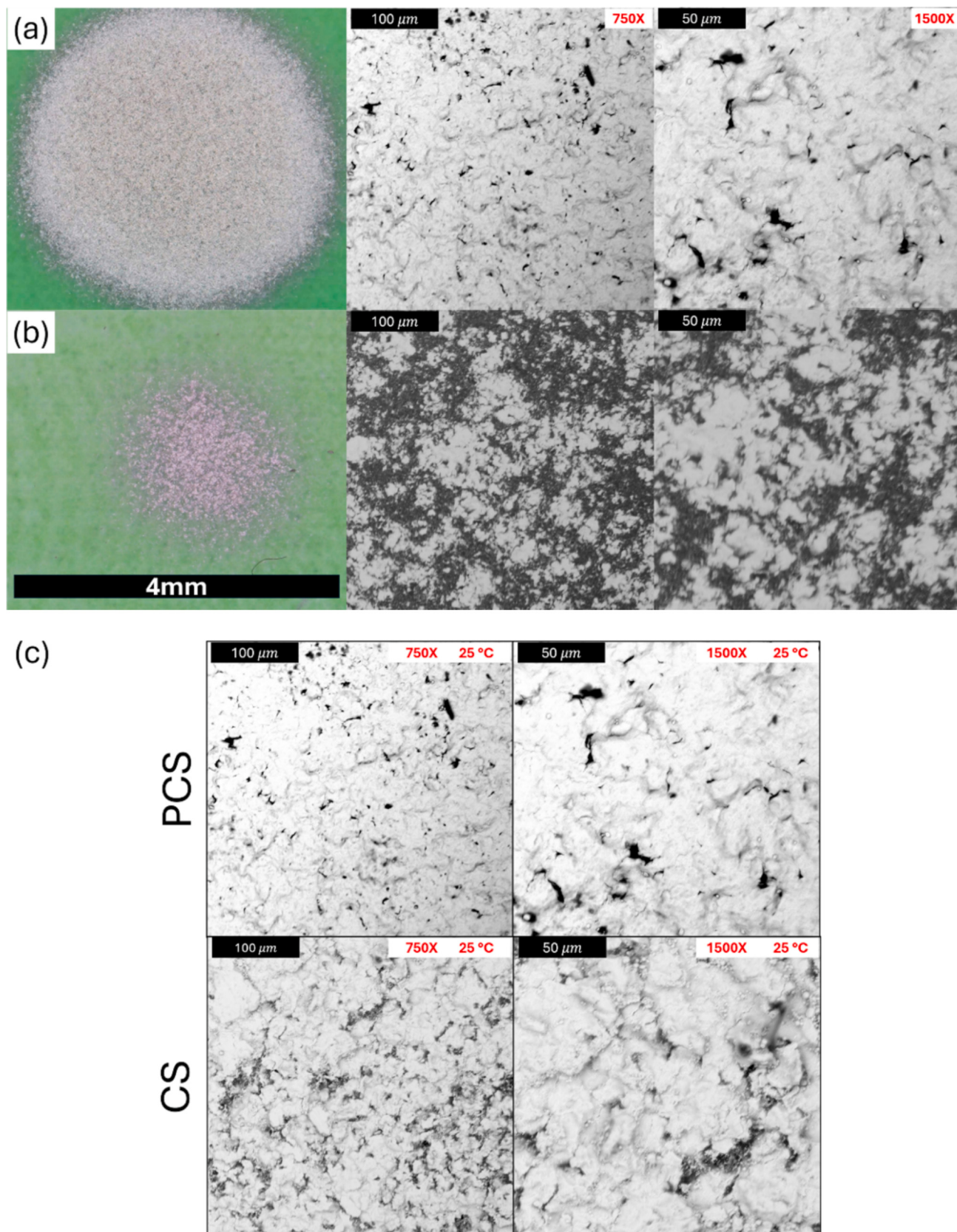


Fig. 14. Analysis of Sn coatings deposited on PET film: (a) Dense PCS coatings created using a 20 mm standoff distance; (b) sparse PCS coatings created using a 30 mm standoff distance; (c) comparison of the coatings created using the PCS (upper panel) and traditional CS (lower panel) under the same operating conditions.

- diamonds recede into the nozzle and do not immediately reform into a normal shock wave.
- The PCS system is able to deposit sparse and dense coatings of Sn on PET film and Cu on Al substrates, operating effectively at inlet pressure up to 12.4 bar. The coating density increased with higher inlet pressure and reduced standoff distances.
  - PCS led to dense coating with remarkably less porous (1.73-fold) compared to CS coatings under the same process settings.

Future works should involve additional analysis and characterization of the PCS system, particularly investigating the effects of nozzle inlet temperature as well as the performance of the PCS system using repeated pulses. Continued development should also prioritize extended operation and implementation of control systems to enhance powder and gas flow within the nozzle, and an analysis of deposition quality on a larger scale should be examined with a focus on optimizing deposition coverage while minimizing the number of pulses. Furthermore, an investigation into understanding the effects of critical nozzle geometry features such as nozzle length, nozzle exit shape, and nozzle expansion ratio should be performed to better understand the effects of these parameters on PCS performance. Additionally, the adhesive strength and durability of PCS coatings should be thoroughly evaluated and compared with traditional CS coatings, while also exploring additional applications for the PCS system.

#### CRediT authorship contribution statement

**Ted Gabor:** Writing – review & editing, Writing – original draft, Methodology, Formal analysis, Data curation. **Yijie Wang:** Visualization, Validation, Data curation. **Semih Akin:** Writing – review & editing, Validation, Methodology, Investigation, Conceptualization. **Fengfeng Zhou:** Writing – review & editing, Methodology, Investigation, Formal analysis. **Jun Chen:** Writing – review & editing, Supervision, Resources. **Yongho Jeon:** Writing – review & editing, Resources, Project administration, Funding acquisition. **Martin Byung-Guk Jun:** Writing – review & editing, Supervision, Resources, Project administration, Funding acquisition, Conceptualization.

#### Declaration of competing interest

The authors declare that they have no known competing financial interests or personal relationships that could have appeared to influence the work reported in this paper.

#### Acknowledgements

This work was supported by the National Research Foundation of Korea (NRF) grant funded by the Korea government (MSIT) (No. RS-2024-00346883).

#### Appendix A. Supplementary data

Supplementary data to this article can be found online at <https://doi.org/10.1016/j.surfcoat.2025.131984>.

#### Data availability

Data will be made available on request.

#### References

- [1] S. Yin, M. Meyer, W. Li, H. Liao, R. Lupoi, Gas flow, particle acceleration, and heat transfer in cold spray: a review, *J. Therm. Spray Technol.* 25 (2016) 874–896.
- [2] S. Yin, P. Cavaliere, B. Aldwell, R. Jenkins, H. Liao, W. Li, R. Lupoi, Cold spray additive manufacturing and repair: fundamentals and applications, *Addit. Manuf.* 21 (2018) 628–650.
- [3] A. Viscusi, A. Astarita, R.D. Gatta, F. Rubino, A perspective review on the bonding mechanisms in cold gas dynamic spray, *Surf. Eng.* 35 (2019) 743–771.
- [4] R. Della Gatta, A.S. Perna, A. Viscusi, G. Pasquino, A. Astarita, Cold spray deposition of metallic coatings on polymers: a review, *J. Mater. Sci.* 57 (2022) 27–57.
- [5] H. Che, A.C. Liberati, X. Chu, M. Chen, A. Nobari, P. Vo, S. Yue, Metallization of polymers by cold spraying with low melting point powders, *Surf. Coat. Technol.* 418 (2021) 127229.
- [6] J.-T. Tsai, S. Akin, F. Zhou, M.S. Park, D.F. Bahr, M.B.-G. Jun, Electrically conductive metallized polymers by cold spray and co-electroless deposition, *ASME Open J. Eng.* 1 (2022).
- [7] R. Lupoi, W. O'Neill, Deposition of metallic coatings on polymer surfaces using cold spray, *Surf. Coat. Technol.* 205 (2010) 2167–2173.
- [8] A. Ganesan, M. Yamada, M. Fukumoto, Cold spray coating deposition mechanism on the thermoplastic and thermosetting polymer substrates, *J. Therm. Spray Technol.* (2013) 1275–1282.
- [9] R. Melentiev, N. Yu, G. Lubineau, Polymer metallization via cold spray additive manufacturing: a review of process control, coating qualities, and prospective applications, *Addit. Manuf.* 48 (2021) 102459.
- [10] V.K. Champagne, Repair of magnesium components by cold spray techniques, in: *The Cold Spray Materials Deposition Process: Fundamentals and Applications*, 2007, pp. 327–352.
- [11] V. Champagne, D. Helfritch, The unique abilities of cold spray deposition, *Int. Mater. Rev.* 61 (2016).
- [12] R.N. Raoelison, Y. Xie, T. Sapanathan, M.P. Planche, R. Kromer, S. Costil, C. Langlade, Cold gas dynamic spray technology: a comprehensive review of processing conditions for various technological developments till to date, *Addit. Manuf.* 19 (2018) 134–159.
- [13] B. Jodoin, P. Richer, G. Bérubé, L. Ajdelsztajn, A. Erdi-Betchi, M. Yandouzi, Pulsed-gas dynamic spraying: process analysis, development and selected coating examples, *Surf. Coat. Technol.* 201 (2007) 7544–7551.
- [14] R.N. Raoelison, Coeval cold spray additive manufacturing variances and innovative contributions, in: P. Cavaliere (Ed.), *Cold-Spray Coatings*, Springer International Publishing, Cham, 2018, pp. 57–94, [https://doi.org/10.1007/978-3-319-67183-3\\_3](https://doi.org/10.1007/978-3-319-67183-3_3).
- [15] J. Villafuerte, D. Vanderzwet, M. Yandouzi, B. Jodoin, Shockwave Induced Spraying, (n.d.).
- [16] M. Yandouzi, H. Bu, M. Brochu, B. Jodoin, Nanostructured Al-based metal matrix composite coating production by pulsed gas dynamic spraying process, *J. Therm. Spray Technol.* 21 (2012) 609–619.
- [17] M. Yandouzi, P. Richer, B. Jodoin, SiC particulate reinforced Al-12Si alloy composite coatings produced by the pulsed gas dynamic spray process: microstructure and properties, *Surf. Coat. Technol.* 203 (2009) 3260–3270.
- [18] M. Yandouzi, E. Sansoucy, L. Ajdelsztajn, B. Jodoin, WC-based cermet coatings produced by cold gas dynamic and pulsed gas dynamic spraying processes, *Surf. Coat. Technol.* 202 (2007) 382–390.
- [19] M. Yandouzi, L. Ajdelsztajn, B. Jodoin, WC-based composite coatings prepared by the pulsed gas dynamic spraying process: effect of the feedstock powders, *Surf. Coat. Technol.* 202 (2008) 3866–3877.
- [20] M. Yandouzi, B. Jodoin, Cermet coatings prepared by pulsed gas dynamic spraying process: effect of the process parameters, *Surf. Coat. Technol.* 203 (2008) 104–114.
- [21] F. Robitaille, M. Yandouzi, S. Hind, B. Jodoin, Metallic coating of aerospace carbon/epoxy composites by the pulsed gas dynamic spraying process, *Surf. Coat. Technol.* 203 (2009) 2954–2960.
- [22] R. Nikbakht, B. Jodoin, Thick Cu-HBN coatings using pulsed gas dynamic spray process: coating formation analysis and characterization, *J. Therm. Spray Technol.* 31 (2022) 609–622.
- [23] R. Nikbakht, R.R. Chromik, B. Jodoin, A novel approach for manufacturing cellular metallic structures using pulsed gas dynamic spraying process, *Addit. Manuf.* 66 (2023) 103473.
- [24] M. Karimi, B. Jodoin, G. Rankin, Shock-wave-induced spraying: modeling and physics of a new spray process, *J. Therm. Spray Technol.* 20 (2011) 866–881.
- [25] M. Karimi, G.W. Rankin, B. Jodoin, Shock-wave induced spraying: gas and particle flow and coating analysis, *Surf. Coat. Technol.* 207 (2012) 435–442.
- [26] G. Huang, D. Gu, X. Li, L. Xing, H. Wang, Numerical simulation on syphonage effect of laval nozzle for low pressure cold spray system, *J. Mater. Process. Technol.* 214 (2014) 2497–2504.
- [27] T. Gabor, S. Akin, M.B.-G. Jun, Numerical studies on cold spray gas dynamics and powder flow in circular and rectangular nozzles, *J. Manuf. Process.* 114 (2024) 232–246.
- [28] F.T. Guide, ANSYS Fluent Theory Guide, ANSYS Inc., USA 15317, 2013, pp. 724–746.
- [29] T.-H. Shih, W.W. Liou, A. Shabbir, Z. Yang, J. Zhu, A new k-e eddy viscosity model for high reynolds number turbulent flows, *Comput. Fluids* 24 (1995) 227–238.
- [30] P. Rosin, E. Rammler, The Laws governing the fineness of powdered coal, *J. Inst. Fuel* 7 (1933) 29–36.
- [31] S.A. Morsi, A.J. Alexander, An investigation of particle trajectories in two-phase flow systems, *J. Fluid Mech.* 55 (1972) 193–208.
- [32] T.C. Jen, L. Li, W. Cui, Q. Chen, X. Zhang, Numerical investigations on cold gas dynamic spray process with nano- and microsize particles, *Int. J. Heat Mass Transf.* 48 (2005) 4384–4396.
- [33] ANSYS Fluent 12.1 User Guide, 2011.
- [34] S. Akin, P. Wu, C. Nath, J. Chen, M.B.-G. Jun, A study on converging-diverging nozzle design for supersonic spraying of liquid droplets toward nanocoating applications, *J. Manuf. Sci. Eng.* 145 (2023).

- [35] B. Jodoin, Cold spray nozzle mach number limitation, *J. Therm. Spray Technol.* 11 (2002) 496–507.
- [36] E.H. Kwon, S.H. Cho, J.W. Han, C.H. Lee, H.J. Kim, Particle behavior in supersonic flow during the cold spray process, *Met. Mater. Int.* 11 (2005) 377–381.
- [37] H. Katanoda, M. Fukuhara, N. Iino, Numerical study of combination parameters for particle impact velocity and temperature in cold spray, *J. Therm. Spray Technol.* 16 (2007) 627–633.
- [38] R.N. Raoelison, Role of the Magnus effect in additive manufacturing at the scale of the micron-sized powders within the supersonic gas flow of cold spraying, *Addit. Manuf.* 97 (2025) 104610, <https://doi.org/10.1016/j.addma.2024.104610>.
- [39] R.N. Raoelison, L.L. Koithara, S. Costil, C. Langlade, Turbulences of the supersonic gas flow during cold spraying and their negative effects: a DNS CFD analysis coupled with experimental observation and laser impulse high-speed shadowgraphs of the particles in-flight flow, *Int. J. Heat Mass Transf.* 147 (2020) 118894, <https://doi.org/10.1016/j.ijheatmasstransfer.2019.118894>.
- [40] T. Klassen, F. Gärtnner, T. Schmidt, J.O. Kliemann, K. Onizawa, K.R. Donner, H. Gutzmann, K. Binder, H. Kreye, Basic Principles and Application Potentials of Cold Gas Spraying, *Materialwissenschaft Und Werkstofftechnik*, John Wiley & Sons, Ltd, 2010.
- [41] S. Akin, Y.W. Kim, S. Xu, C. Nath, W. Wu, M.B.G. Jun, Cold spray direct writing of flexible electrodes for enhanced performance triboelectric nanogenerators, *J. Manuf. Process.* 100 (2023) 27–33.